UNIVERSITY OF HELSINKI   REPORT SERIES IN PHYSICS

HU-P-D172

Multiscale study on hydrogen mobility in metallic fusion divertor material

Kalle Heinola

Division of Materials Physics
Department of Physics
Faculty of Science
University of Helsinki
Helsinki, Finland

ACADEMIC DISSERTATION

To be presented, with the permission of the Faculty of Science of the University of Helsinki, for public criticism in the Auditorium D101 of the Department of Physics (Physicum), on April 16th, 2010, at 12 o'clock p.m.

HELSINKI 2010

ABSTRACT

For achieving efficient fusion energy production, the plasma-facing wall materials of the fusion reactor should ensure long time operation. In the next step fusion device, ITER, the first wall region facing the highest heat and particle load, *i.e.* the divertor area, will mainly consist of tiles based on tungsten. During the reactor operation, the tungsten material is slowly but inevitably saturated with tritium. Tritium is the relatively short-lived hydrogen isotope used in the fusion reaction. The amount of tritium retained in the wall materials should be minimized and its recycling back to the plasma must be unrestrained, otherwise it cannot be used for fueling the plasma. A very expensive and thus economically not viable solution is to replace the first walls quite often. A better solution is to heat the walls to temperatures where tritium is released. Unfortunately, the exact mechanisms of hydrogen release in tungsten are not known.

In this thesis both experimental and computational methods have been used for studying the release and retention of hydrogen in tungsten. The experimental work consists of hydrogen implantations into pure polycrystalline tungsten, the determination of the hydrogen concentrations using ion beam analyses (IBA) and monitoring the out-diffused hydrogen gas with thermodesorption spectrometry (TDS) as the tungsten samples are heated at elevated temperatures. Combining IBA methods with TDS, the retained amount of hydrogen is obtained as well as the temperatures needed for the hydrogen release.

With computational methods the hydrogen-defect interactions and implantation-induced irradiation damage can be examined at the atomic level. The method of *multiscale* modelling combines the results obtained from computational methodologies applicable at different length and time scales. Electron density functional theory calculations were used for determining the energetics of the elementary processes of hydrogen in tungsten, such as diffusivity and trapping to vacancies and surfaces. Results from the energetics of pure tungsten defects were used in the development of an classical bond-order potential for describing the tungsten defects to be used in molecular dynamics simulations. The developed potential was utilized in determination of the defect clustering and annihilation properties. These results were further employed in binary collision and rate theory calculations to determine the evolution of large defect clusters that trap hydrogen in the course of implantation. The computational

results for the defect and trapped hydrogen concentrations were successfully compared with the experimental results. With the aforedescribed multiscale analysis the experimental results within this thesis and found in the literature were explained both quantitatively and qualitatively.

Contents

1 INTRODUCTION

Energy production from the fusion of light mass particles has been under extensive study for the past 50 years. Fusion power is an energy production method which in principle can provide energy for mankind with nearly unlimited energy reserves and, as a base load provider, it fits well into the future mix of sustainable energy sources. In addition, fusion energy has other benefits, such as inherent safety, no emission of harmful greenhouse gases, a reasonable economical load, and produce no long-lived radioactive waste. A decisive step towards feasible fusion energy production was taken in 2005, when the construction site for the international thermonuclear experimental reactor, ITER, was agreed (Fig. 1) [1, 2].

Still today many open questions exist concerning the materials science of the suitable materials candidate for the incomparable conditions present in the course of the ITER operation. Therefore the fundamental interaction mechanisms of the fusion fuel, *i.e.* the plasma, with the surrounding wall material need to be exhaustively examined. The importance of understanding the behaviour of the material is even further emphasized when the knowledge from the ITER experiments will be extrapolated to the plasma conditions of the first commercial test reactor for fusion DEMO [3].

The fuel inside a thermonuclear reactor consists of plasma of hydrogen (H, ^{1}H, protium) and its isotopes deuterium (D, ^{2}H) and tritium (T, ^{3}H). The energy is gained from the fusion of these elements: I) $D + T \rightarrow {}^4He + n$ is the main reaction of the D-T fuel, II) $D + D \rightarrow T + H$ and III) $D + D \rightarrow {}^3He + n$ are minor reactions with nearly equal branching ratios. The mean energy of the hydrogen ions in the plasma core is ~ 30 keV, which corresponds to a temperature of $\sim 100 \times 10^6$ K. Due to the reactions I)-III), energetic neutrons are emitted that in turn give up their energy as heat to the outermost part of the surrounding wall material. Part of the neutrons react with lithium (Li) in the blanket wall and as a result, new T fuel from the reaction $Li + n \rightarrow T + {}^4He$ is produced. This conversion of Li to T, also called tritium breeding, increases the efficiency of the fusion device. The objective efficiency of ITER is 10 [4].

The plasma is magnetically confined but due to its demanding controllability and the non-homogeneity of the magnetic field lines, the plasma will be in a constant interaction with the inner surrounding walls of the reactor, *i.e.* the vacuum vessel blanket modules and the divertor region (Fig. 1). Due to the interactions, a fraction of the hydrogen species can get trapped in the wall material and be lost from the plasma. Moreover, the wall material can erode, which leads to particles being ejected to the plasma. These impurities will induce radiation losses that depend on the atomic number, Z, of the impurity according to $\sim Z^2 - Z^4$. These energy losses will in turn create instabilities in the plasma, which can lead to undesired rapid quenching of the plasma pulse. In other words
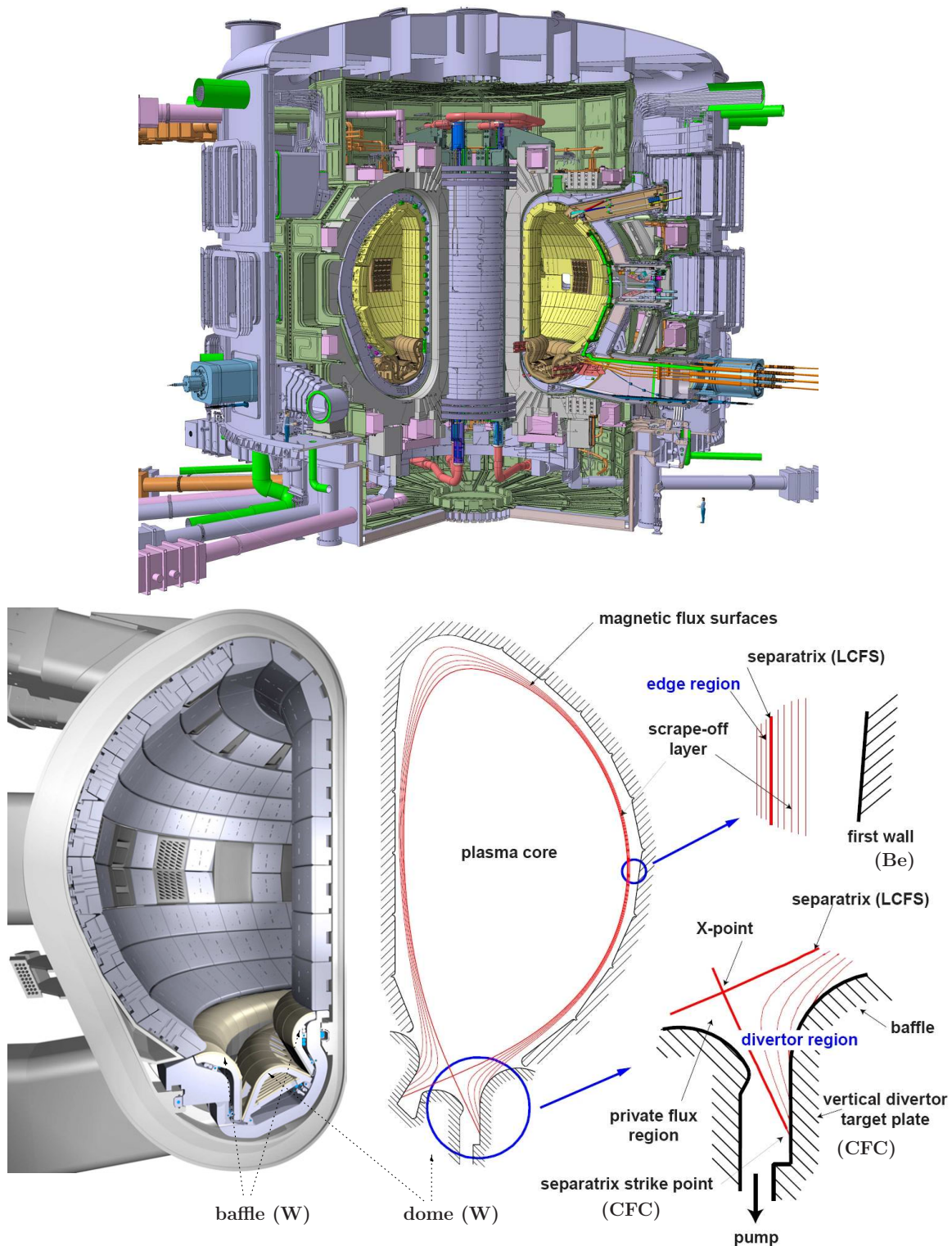
Figure 1: (Top) Cutaway of the conceptual design of the next step fusion device ITER [1]. (Bottom: left) Cross-section of the vacuum vessel showing the baffle and dome areas on the divertor [1]. (Bottom: right) The scrape-off layers of the magnetic field lines of the plasma [5]. The charged particles escaping the plasma orbit on the outer magnetic field lines and interact with the blanket first walls (Be) ending up in the divertor region (W, CFC) giving high heat and particle load.

the wall materials must be sufficiently poor hydrogen getters and have a long lifetime under particle bombardment.

Charged low-energy ($1 - 100$ eV) hydrogen and high-energy helium (He) ions formed as by-product in the fusion reactions, will be orbiting on the outer field lines after escaping the plasma core. The highest particle flux and thermokinetic load will be subjected to the lower part of the vessel, where the magnetic lines are crossed and form a separatrix region (Fig. 1). The divertor plates under the separatrix region must withstand a high heat and particle load from the plasma. The most promising metallic candidate material to be used as the divertor plasma-facing wall material (PFM) is tungsten (W) which is the study subject of this thesis. The W plates will be placed on the dome and baffle areas of the divertor. Benefits of W are that it has the highest melting point of all metals and low erosion rate. Nonetheless, since W is a high-Z material the number of W particles ejected in the plasma must be minimized.

The hydrogen and He congregate on the W surface or, when having high energies or high fluxes, penetrate through it and diffuse deeper into the bulk. These solute light elements have a low solid solubility but a high mobility in W. The hydrogen isotopes and He can easily be immobilized by other impurity atoms present in the lattice, on the surfaces of the grain boundaries, at dislocations and voids, or by other lattice imperfections that can act as active trapping sites. The accumulation of hydrogen and He into these traps can lead to modification of the material's mechanical and physical properties. How He influences W is presently studied intensively both computationally and experimentally by several international groups. So far no extensive studies with modern computational resources in combination with detailed experimental work have been carried out for hydrogen in W.

In addition to tungsten, other PFM candidates are the carbon-based fiber composite (CFC) materials and beryllium (Be). The CFC materials are low-Z materials and will be used in the vertical target areas, *i.e.* the strike points of the divertor, where the highest particle load will be subjected. A disadvantage of carbon is that it efficiently traps hydrogen species and has a high sputtering yield. Moreover, the eroded carbon can be re-deposited in remote areas where it will form hydrogen-containing carbon thin-films. Low-Z metal Be will be placed into the blanket modules that will cover the interior wall of the vacuum vessel. Be removes impurities such as oxygen from the plasma, but it is easily eroded. The blanket modules and the divertor region are the most critical components of the fusion device from the first wall viewpoint since they are directly facing the plasma.

The high flux of neutrons from the fusion reactions can, after being absorbed, transmutate a fraction of the W atoms into rhenium (Re) and further to osmium (Os). Recent experimental studies on D trapping in Re-doped W have indicated that the Re atoms do not act as an active trapping site for

hydrogen [6]. Still, the theoretical explanation of the presence of Re and Os affecting the bulk W and the hydrogen retention in W is still missing.

Since the plasma fuel is interacting with the wall material, it is a necessity to have fundamental knowledge of the processes occurring on the surface and inside the wall material, in particular the hydrogen retention, recycling, and release. The accumulation of the hazardous tritium is an environmental issue to be considered in the long-term ITER operation.

2 PURPOSE AND STRUCTURE OF THIS STUDY

The purpose of this thesis is to investigate the migration and retention properties of hydrogen in tungsten both experimentally and computationally. In general, the results improve understanding of the behaviour of hydrogen in metals.

The thesis consists of this summary and six publications, either published, accepted for publication, or under consideration for publication in international peer-review journals. The six publications are referred to by bold-face Roman numbers. These original publications are included at the end of the summary.

The summary consists of seven sections. In this section the summary of the publications is given and the contribution of the author is explained. In Sect. 3 the basic concepts and the background of the main subject of this thesis is outlined. The experimental and computational methods used in this study are presented in Sect. 4. The main results of the hydrogen diffusion are given in Sect. 5. In Sect. 6 results pertaining the hydrogen retention and trapping properties are presented. The conclusions are given in Sect. 7.

2.1 Summaries of the original publications

In Publication **I** the experimental methods to determine the deuterium implantation profiles in tungsten are presented. Results for the deuterium out-diffusion temperatures are given. The implantation energy dependency to the retained deuterium concentration profiles is studied in Publication **II**. Results for hydrogen diffusivity in tungsten as obtained from density functional theory calculations are presented in Publication **III**. In Publication **IV** the bond-order potential for describing extended and point defects in tungsten is presented. The surface properties of tungsten and the hydrogen migration on tungsten surface have been investigated computationally with density functional theories in

Publication **V**. Computational results of hydrogen trapping to point defects in tungsten are given in Publication **VI**.

Publication I: Quantification of deuterium irradiation induced defect concentrations in tungsten,

T. Ahlgren, K. Heinola, E. Vainonen-Ahlgren, J. Likonen and J. Keinonen, *Nuclear Instruments and Methods in Physics Research B* **249**, 436 (2006).

> Deuterium retention in the implantation-induced defects in polycrystalline tungsten was studied. The implantation energy used was chosen to produce defects deep in the sample, thus avoiding surface effects. The retained deuterium concentrations were analyzed with nuclear reaction analysis and secondary ion mass spectrometry. Four different defect types that trap deuterium with release temperatures of 455, 560, 663 and 801 K were observed.

Publication II: Deuterium irradiation-induced defect concentrations in tungsten,

K. Heinola, T. Ahlgren, E. Vainonen-Ahlgren, J. Likonen and J. Keinonen, *Physica Scripta* **T128**, 91 (2007).

> The dependency of the deuterium retention on the implantation energy was investigated. The implantation dose was kept constant. Annealings were carried out at four pre-determined temperatures corresponding to four different defect types that trap deuterium. A quantitative number of each defect type produced by different implantation energies of 5, 15 and 30 keV/D was obtained. Traps with higher detrapping temperatures were observed to be formed closer to the surface.

Publication III: Diffusion of hydrogen in bcc tungsten studied with first principle calculations,

K. Heinola and T. Ahlgren, *Accepted for publication in Journal of Applied Physics* **107**, (2010).

> The hydrogen diffusivity in bulk tungsten was studied. Hydrogen has low solubility and occupies the tetrahedral interstitial site. The hydrogen diffusion coefficient was evaluated using the harmonic transition state theory. It was found that trapping has a strong effect on the experimental diffusivities even up to 1500 K. At low temperatures, taking into account the tunneling correction provided much better agreement with the experimental diffusivity at 29 K than the extrapolated experimental diffusivity result from the high temperature measurements.

Publication IV: Bond-order potential for point and extended defect simulations in tungsten,

T. Ahlgren, K. Heinola, N. Juslin and A. Kuronen, *Journal of Applied Physics* **107**, 033516 (2010).

A reactive interatomic bond-order potential parameter set for tungsten was presented. Special attention in the potential development was given to obtaining the accurate formation and migration energies for point defects, making the potential useful in atomic scale simulations of point and extended defects. With this potential several intrinsic defect properties in W were obtained, *e.g.* the binding energies and clustering radii of vacancy clusters and the annihilation radius of the Frenkel pair.

Publication V: First-principles study of H on the reconstructed W(100) surface,
K. Heinola and T. Ahlgren, *Physical Review B (Brief Reports)* **81**, 073409 (2010).

First-principles calculations were used to study the hydrogen energetics on the (100) tungsten $(\sqrt{2} \times \sqrt{2})R45°$ surface. At low coverages the majority of hydrogen surface diffusion events take place via the short bridge sites. The calculated hydrogen diffusivity agreed with the experimental results, giving an unambiguous description to the diffusion mechanism. The energetics for hydrogen penetration from the surface to the solute site in the bulk was defined. It was found that the bulk-like hydrogen migration took place at depths beyond the second subsurface layer.

Publication VI: Hydrogen interaction with point defects in tungsten,
K. Heinola, T. Ahlgren, K. Nordlund and J. Keinonen *Submitted to Physical Reviev B (Rapid Communications)* (2010).

The trapping properties of hydrogen to point defects in tungsten, *i.e.* the monovacancy, self-interstitial atom, the Re and Os impurities, were studied by first-principles calculations. In determining the hydrogen trapping energies, the zero-point vibrational properties of the hydrogen atom were taken into account. It was found that the vacancy can hold up to five hydrogen atoms at room temperature whereas the self-interstitial is not an attractive trapping site for hydrogen. However, hydrogen distorts the self-interstitial geometry which in turn may enhance the dislocation evolution. The Os interstitial was found to increase the hydrogen inventory in W.

2.2   Author's contribution

The experimental part of this thesis was conducted at the Ion Beam Analysis Laboratory of the University of Helsinki and at the Technical Research Center of Finland. The supercomputer of the Center for Scientific Computing, Espoo, and the computer clusters of the University of Helsinki were employed in the computational part. The author had the main responsibility for the experiments and

analyses in Publications **I** and **II**. The author carried out the density functional calculations in Publications **III** – **VI**. Publications **II**, **III**, **V** and **VI** were written by the author in their entirety. The author wrote part of the Publications **I** and **IV**.

3 HYDROGEN INTERACTIONS WITH PLASMA WALL MATERIALS

The recycling and retention of hydrogen in the inner wall material of the vacuum vessel, *i.e.* the blanket first wall and the divertor region, is of key interest to feasible fusion device operation. In addition, environmental issues have to be considered since the hydrogen isotope T is a β^- active nucleus, which once retained in the wall material, it will have an elevating impact on the emitted radiation of the surrounding structures. An on-site limit of 700 g of T has been set for ITER [7]. This issue concerns mainly the operating personnel of the fusion device, since T is a short-lived nucleus with a half-life of 12.3 years.

In the next sections the basic hydrogen interactions with the plasma-facing wall are outlined. The review is limited to the point of view of the materials' science and therefore no plasma diagnostics are discussed. The *pro et contra* of the material candidates are discussed in these sections.

3.1 Reflection

Ions and neutral particles from the plasma can be reflected from the wall material and be driven back to the plasma. The reflection does not occur necessarily right on the surface of the material but after scattering processes with the host nuclei in the material's crystal lattice. If the energy of the backscattered particle is above the binding energy to the surface, it may escape the material. Due to the conservation of momentum in the backscattering process, the reflection probability increases with the mass of the target material. For example, the particle reflection coefficient R_n for the $1-100$ eV H atoms escaping the plasma is > 0.7 for H on W obtained with Monte Carlo calculations using the binary collision model, whereas the R_n for H on C was found to vary between $0.2-0.5$ [8]. It has been shown experimentally that the surface temperature and the *a priori* H impurity content on the surface have a decreasing effect on reflection [9].

3.2 Hydrogen inventory

3.2.1 Implantation

When the incoming particle is not reflected, it can penetrate further into the material and get implanted. After subsequent scattering processes, the particles slow down because they lose energy by electronic stopping and atomistic collisions [10]. At the fusion relevant temperatures the hydrogen atoms in W are not retained in the solute interstitial sites, since the migration barrier for diffusion is low (Publication **III**). The hydrogen atoms either diffuse out of the material or are immobilized by some impurity atoms in the lattice, on the surfaces of the grain boundaries, at dislocations and voids, or by other lattice imperfections that can act as active trapping sites. The implanted hydrogen can also form a hydride with the host atoms. In the course of ion implantation, different implantation-induced defects can also be formed. Collisions with energies above a certain threshold can kick the host atoms from their lattice sites and thus form Frenkel pairs. A Frenkel pair consists of the self-interstitial atom (SIA) and a vacant lattice site. With high collision energies, the displaced SIAs can create further displacements or even cascades of them. As a result the implantation-induced defects consist of SIAs and vacancies as well as clusters of them and other dislocations in the lattice. Hydrogen retention in the material is affected by the energy of the incoming particle, the net damage present in the material, and the presence of trapping impurities.

An important difference between He and hydrogen self-trapping is that He is found to be trapped by binding to another He at a solute site, as shown by several experiments and computational studies [11], whereas hydrogen is not self-trapped according to jellium model calculations [12] and recent DFT calculations [13, 14] (Publication **III**).

3.2.2 Neutron irradiation

The high flux of neutrons from the fusion reactions can increase the number of hydrogen trapping defects in the surrounding wall materials in addition to the naturally existing or implantation-induced trapping sites [15]. The neutron-induced damage mechanism can have the same evolution as the damage initiated by implantation. Estimates on T retention in W have shown an enhancement up to a factor of 8 due to the neutron damage. Currently, the exact microstructure evolution due to the neutron irradiation and its influence on hydrogen trapping is unknown [7].

In addition, the neutrons can have an impact on the deformation of the surrounding wall material. The maximum energy of the incoming neutrons is 14 MeV, but the energy spectrum is not discrete. Although the majority of the neutrons have no other than collision interactions with the PFM's, the

low energy neutrons (1 eV - 10 keV) can get absorbed within the W material. After the absorption, the unstable W daughter nucleus converts to Re via β^--emission. In the presence of the incoming neutron flux, the Re atoms can further lead to the formation of Os. Estimates for the ITER environment have given impurity concentrations of $\simeq 2\%$ and $\simeq 0.03\%$ to Re and Os in the W divertor plates [16, 17]. Recent experimental studies on W-Re and W-Re-Os alloys have shown that the enrichment of W with Re and Os can lead to hardening and embrittlement of W [18, 19].

3.3 Erosion

3.3.1 Sputtering

Sputtering of the material is a process in which atoms or molecules are detached from the surface due to the bombardment by the incoming particles. The lifetime of the first wall materials is determined by their ability to withstand sputtering.

Sputtering can be divided into chemical and physical sputtering [20, 21]. Chemical sputtering occurs when the incoming particle forms a chemical compound with the surface atoms which in turn lowers the binding energy of the surface atoms and the compound comes off the surface. In other words, chemical sputtering depends on the electronic tendency of the host material to chemically bond with the bombarding particles. Therefore, chemical sputtering is highly dependent on the material as well as on temperature. Physical sputtering is present in all materials independent of their structure. In physical sputtering, the kinetic energy of the incoming particle is transferred to the atoms on the surface layers. This can break bonds between the host atoms, which leads to emitted particles from the surface.

Interaction between hydrogen and carbon enhances the chemical erosion of CFC material. Substantial amounts of eroded hydrogenated carbon material can be deposited to large areas inside the vacuum vessel. Moreover, the re-erosion of the deposited carbon layers or thin films is found to be an order of magnitude higher than that for bulk graphite [22]. The stability of these thin carbon films depends on their hydrogen concentration [23]. The efficient trapping of T in CFC and the migration of hydrocarbons increase the T content in the wall materials. Be has a high physical sputtering rate and it melts easily [24]. The Be erosion rate can be similar to CFC. The erosion of W is an order of magnitude lower than of Be [25].

3.3.2 Blistering

Even though W has a low sputtering yield under hydrogen bombardment, large amounts of W can be eroded via the blistering mechanism. Blistering of the material takes place under high implantation fluences and fluxes [26]. It is initiated by continuous bombardment of the material as the implanted ions agglomerate together and displace the host atoms from their lattice sites, forming larger cavities and eventually bubbles. The bubble formation near the surface can be seen as blister formation on the surface topography. This induces stress to the lattice that can be released via rupturing of the blister. The mechanims of blister formation due to hydrogen implantation is somewhat unclear since the measured thicknesses of the blister covers, *i.e.* the *deckeldicke*, are several orders of magnitude larger than the projected range of the implanted hydrogen ions [27]. This might be due to stress resulting from the disproportion of the implanted ions and the implantation-induced defects in the material as a function of depth [28]. In addition, the blister sizes have been reported to vary with the sample exposure temperature [29] and with the implantation history of the sample [30]. However, He-induced blisters are known to be formed at the depth of the projected range [31]. In a fusion device the rupturing result in emission of the W wall material which will have a serious impact on the power loss of the plasma.

3.3.3 Large scale erosion

In ITER, a number of abnormal events are expected to be present during the plasma operation. Two main abnormal events are the edge localised modes (ELMs) and disruptions. In these events a large amount of energy stored in the plasma is released to the walls within short time scales. The ELMs are instabilities of the outer region of the core plasma that release $50 - 80\%$ of the core energy to the divertor. The disruptions occur after the plasma has become instable and is terminated rapidly. During the disruption the divertor target material and nearby surfaces will evaporate and melt. No material known today can withstand the energy load from ELMs and disruptions [5].

4 METHODOLOGY

In this section the methods used in this thesis are outlined. These are based on both experimental and computational methods. The experimental contribution consists of hydrogen implantations and profiling of the retained hydrogen concentrations with the secondary ion mass spectrometry and nuclear reaction analysis methods. Thermodesorption spectrometry was performed for determining the hydrogen dissociation temperatures from different trap types. The computational part is composed

of developing a bond-order potential for obtaining the properties of intrinsic defects in W and of calculations based on electron density functional theory for hydrogen energetics in W. More details are found in the cited Publications given in each section.

4.1 Deuterium implantations

The hydrogen retention was studied by D^+ implantations into W. The D isotope was used, since its signal is easily separated from the ^{1}H background, that is naturally present in every experimental system. T was not considered to be used due to its radioactivity. In the implantations and in the subsequent analyses described in the following subsections, the vacuum pressure was in the $10^{-8} - 10^{-7}$ mbar range. The major part of this total pressure comprised of the partial pressures of H_2, N_2, H_2O and CO_2 and their refractory patterns as measured with quadrupole mass spectrometer (QMS). The natural abundance of D is 0.015 at.% compared to 100 at.% of H. This ensures that the subsequently measured D signals originated solely from the implanted D^+ ions in the samples.

The samples were high purity (99.99%) polycrystalline W with a thickness of 1 mm. The size of the samples was 15×10 mm^2 and they were cut out from a larger W sheet. The mirror-polished samples were measured to have a surface roughness of less than 10 nm (root mean square). In order to reduce the mean grain size, the samples were pre-annealed at about 1370 K for 1 h prior to the implantations. All the implantations were carried out at room temperature (RT).

The D^+ implantation energies used in this study were 5, 15 and 30 keV. These energies are too high to mimic the impinging hydrogen energies in the fusion device but are suitable for fundamental studies on trapping effects. It was evident that the implantation energies used would produce implantation-induced traps, *e.g.* for 5 keV D in W the maximum recoil energy is ~ 0.2 keV which is above the experimental W displacement energy of ~ 42 eV [32]. The mean projected range of 100 eV D in W, $R_p \sim 3$ nm, is of the same order than the measured sample surface roughness, whereas implantation with 5, 15 and 30 keV increase R_p to 36, 86 and 155 nm, respectively [33]. Implantations with the abovementioned energies ensured that the implanted D was a long way below the surface roughness, so the surface should not influence the determination of the D concentration profiles.

The implantation dose used in the experiments was 5.8×10^{16} D/cm^2. This value corresponds to a maximum concentration of 5 at.% if all the implanted ions would be retained in the sample. The dose used is high enough for statistically accurate post implantation ion beam analyses, but low enough to avoid the blistering effect. Blistering takes place for hydrogen implantation at doses of $> 10^{19}$ cm^{-2} [27].

4.2 Thermodesorption spectrometry

With thermodesorption spectrometry (TDS) the dynamics of the out-diffusing hydrogen atoms can be monitored *in situ*. Estimates on the associated energy, *e.g.* the dissociation energy of hydrogen from a defect in the bulk, can be determined from the corresponding release temperature.

As the temperature of the sample is raised, thermally activated hydrogen atoms get dissociated from the traps in the bulk and start to diffuse further into the bulk or end up at the sample surface. On the surface, the hydrogen atom is trapped to an adsorption site with an energy of E_{ads} (Fig. 7). When two hydrogen atoms come on the same surface site, they can recombine and form a molecule $H_{2,surf}$, which is loosely bound to the surface and rapidly desorbs into the gaseous phase $H_{2,g}$. The recombination process can be expressed as

$$H_{surf} + H_{surf} \stackrel{k_{des}}{\rightarrow} H_{2,surf} \stackrel{k'_{des}}{\rightarrow} H_{2,g}. \tag{1}$$
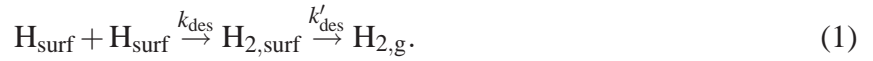
The rapid desorption indicates that the rate $k'_{des} \gg k_{des}$. The desorption rate, measured with TDS, is then

$$\frac{d[H_{2,g}]}{dt} = k_{des}[H_{surf}]^2, \tag{2}$$

where $d[H_{2,g}]/dt$ is the desorption rate of H_2 molecules and $[H_{surf}]$ is the hydrogen atom surface concentration. The recombination follows *second* order kinetics (β_2 phase). The k_{des} is expressed as $k_{des} = \nu_2(\theta)\exp(-E_{des}(\theta)/kT)$, where ν_2 is a pre-exponential factor, θ is the surface H coverage and E_{des} the energy needed for molecular desorption. For hydrogen on transition metal surfaces, E_{des} can be approximated with the atomic adsorption energy as $E_{des} \approx 2E_{ads}$ [34].

The *first* order desorption (β_1 phase) takes place when all the surface sites for the second order desorption are occupied. Now $k'_{des} \ll k_{des}$ and hydrogen desorbs directly as H_2. The desorption rate is expressed as

$$\frac{d[H_{2,g}]}{dt} = k'_{des}[H_{2,surf}], \tag{3}$$

with $k'_{des} = \nu_1(\theta)\exp(-E_{des}(\theta)/kT)$ for the first order kinetics. The β_2 and β_1 are considered as the main coverage phases for atomic and molecular hydrogen on tungsten, respectively ($\sim$ 90% of adsorbed hydrogen), although other phases have been experimentally reported, *i.e.* the α and γ phase, which are present at RT and below [35, 36]. However, the origin of these phases is not well understood.

As can be seen from Eq. (2), the experimentally measured hydrogen output from the surface depends strongly on the surface conditions. That is, if the detrapping energy of atomic hydrogen in the bulk,
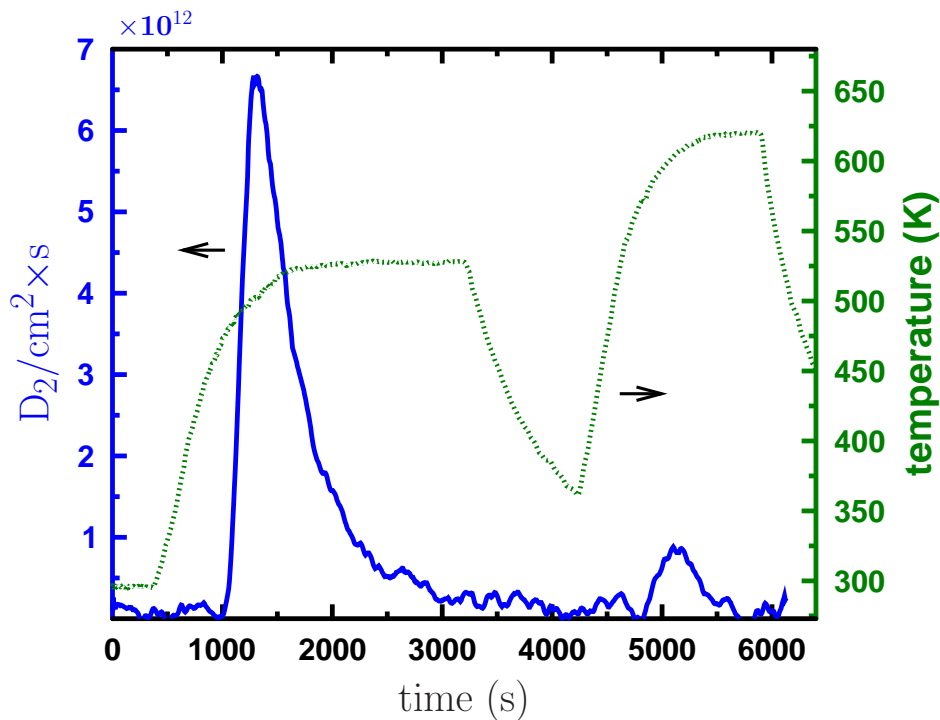
Figure 2: The measured TDS signal for desorbed D_2 from W showing two peaks corresponding to two separate traps in the bulk. From Publication **II**.

E_{trap}, is lower than or nearly the same as E_{ads}, a continuous agglomeration of atomic hydrogen to the surface takes place and H_{surf} increases, but no desorption of hydrogen is necessarily present [37]. In other words, the surface can act as a desorption limiting step. This can be avoided with sufficient hydrogen reserves diffusing from the bulk to the surface, because E_{des} decreases as θ increases and faster desorption is achieved [38].

The D implanted W sample annealings were performed in a quartz-tube furnace in high vacuum and details are found in Publications **I** and **II**. The TDS was carried out as follows. After the implantations the samples were annealed according to certain set of temperature profiles for emptying each hydrogen trap type individually. The annealing temperature of the sample was carefully elevated until the desorption peak, *i.e.* the TDS signal corresponding to a specific trap type, reached its maximum. Beyond the TDS maximum the temperature was kept constant until the TDS signal dropped back to null. The TDS signal dropping to zero, although the sample was kept above detrapping temperature, indicates that the trap type in question was completely emptied from D atoms. In this way it was possible to empty each trap type present in the W sample one at a time. This is clearly seen in Fig. 2 where the TDS signal reaches its maximum at a specific trap and then drops to zero as all the D was released from this trap. To empty the next trap of D, the annealing procedure is repeated with the corresponding temperature. This can be seen as the second peak in the TDS spectra in Fig. 2. After

emptying the trap studied, the retained D concentration was determined with ion beam analyzes and compared with the areal concentration of the TDS signal.

The isothermal annealing used in this study allows a detailed study of each specific trap type, since signals from other traps are not born. This method differs from the normally used annealing procedure where the temperature is raised with a constant slope to some pre-determined final temperature. Typical heating rates used elsewhere range from 10 K/s to 10 K/min and the final temperatures are usually high enough for emptying all the traps during a single heating.

4.3   Secondary ion mass spectrometry

An implementation of the sputtering in materials analysis is the secondary ion mass spectrometry (SIMS). SIMS is sensitive for dopants and impurities of all isotopes from H to U. The sputtering is accomplished by etching with heavy projectiles, *e.g.* O^+, O_2^+, Ar^+, Cs^+, Kr^+ or Xe^+, in the energy range of $1 - 50$ keV. A fraction of the sputtered particles is ionized and the masses are measured with a mass spectrometer *in situ* as a function of time. The depth scale of the impurity concentration profile is deduced by measuring the depth of the final sputtering crater accurately and by calculating the sputtering rate of the host matrix. The latter is achieved by calibration tests for the sputtering rate dependence on the sample composition. The impurity concentration profiles deduced with SIMS can be influenced by well-known artifacts, *e.g.* charging effects, selective sputtering, memory effect, etc., which has to be eliminated in order to obtain reliable undistorted impurity profiles [39–41].

SIMS was used in Publications **I** and **II** for determining the D profiles as a function of depth in the as-implanted and the subsequently annealed W samples. The studied samples were high purity W and the D impurity concentration was low so the deviation in the sputtering rate was minimized. In Publication **I** the SIMS measurements were done using 12 keV Cs^+ primary ions and in Publication **II** with 5 keV O_2^+ with ion currents of 150 and 250 nA, respectively. In both analyses, the analyzed area was 290×430 μm^2 and the uncertainty of the crater depth was estimated to be 10%. The measured D profiles were calibrated to absolute concentration values with the results obtained from nuclear reaction analysis.

4.4   Nuclear reaction analysis

Nuclear reaction analysis (NRA) was used for determining the number of implanted deuterium ions in the tungsten samples. The quantitative values obtained were used for calibrating the D depth profiles obtained with SIMS.

In NRA an energetic projectile penetrates into the bulk and if the energy is suitable between the colliding nuclei, a nuclear reaction of the nuclear species may occur. The mass deficit in the reacting system together with the geometry of the experimental setup determine the kinetics of the resulting daughter nuclei which are detected.

The NRA measurements in Publications **I** and **II** were carried out by exploiting the D(^{3}He,p)^{4}He nuclear reaction. A reference sample for calibrating the D concentrations was prepared by implanting 30 keV D_2^+ ions to a fluence of 7.5×10^{16} 1/cm^2 into silicon, where D is known to be immobile [42]. The D(^{3}He,p)^{4}He reaction has a relatively broad differential cross-section peak of $\sim$60 mb/sr near 640 keV of the incoming ^{3}He energy [43, 44]. At ^{3}He energies below 1.2 MeV, the differential cross section is angle independent [44–46]. A 700 keV ^{3}He^{2+} collimated beam with a diameter of 2.0 mm was used. The incident angle to the sample normal was 40°. A 4 μm thick Al foil was put in front of the 1500 μm thick wide-angle silicon detector to stop the backscattered ^{3}He. The solid angle of the detector was 0.19 sr and it was placed at 60° relative to the incident beam. Protons with an energy of 13.7 MeV from the D(^{3}He,p)^{4}He reaction were collected for the analysis. The aperture width of the detector ($\pm 12°$) caused a ± 250 keV geometrical straggling to the detected protons. The Al foil caused a minor additional energy straggling of about 4.9 keV. It is worthwhile to emphasize that neither the large solid angle of the detector nor the energy spread had any effect in the analysis of the NRA spectra since only the total number of counts in the proton peak area were of interest.

4.5 Molecular dynamics

Computer simulations of large systems need a computationally efficient description of the atomic interactions. Calculations based on molecular dynamics (MD) simulations are an efficient tool to describe atomic systems and their properties classically. With MD systems up to millions of atoms can be studied with a simulation timescale of nanosecond. Interatomic forces and the kinetics of the system are obtained with an analytical potential energy function which has been tailored for describing reliably the selected properties of the system studied.

As a part of this thesis, a potential parameter set for the previously constructed bond-order potential (BOP) [47, 48] was obtained which, in addition to the bulk properties, also gives accurate formation and migration energies for point defects in W (Publication **IV**). This parameter set can later be used in numerous atomistic simulations including interpretation and simulation of recovery stages in the irradiated W and simulation of extended defects. In Publication **IV** the obtained BOP parameter set was applied to find the configuration, the trapping radii and the binding energies for W vacancy clusters and the recombination radius for a self-interstitial atom and a monovacancy. Moreover, the

developed BOP has been used to obtain D-implantation-induced damage in W in which the D is trapped.

4.6 Density functional theory

Calculations based on electron density functional theory (DFT) can be considered as a state-of-the-art theoretical research method in the fields of material physics and chemistry [49, 50]. Density functional theories are based only on the knowledge of the electronic structure of the material's atoms and are recurrently called as an *ab initio* method despite the functionals by itself are parametrized. As a result, all the physical and chemical properties of the system can be determined up to a certain extent. DFT calculations have their limitations due to the restricted validity of the functionals used and because the number of atoms that can be considered in a study is bounded by the computational power available. In a modern computing cluster environment, systems up to hundreds of atoms can be examined. Since even these are only microscopical systems compared to average experimental entities ($\sim 10^{22}$ atoms/cm^3), the DFT results must undergo careful validation when extrapolated into larger realistic dimensions. On the other hand, DFT calculations can give insight and detailed information about systems which are not directly approachable experimentally.

DFT calculations were used for computing the total energies of the studied systems. Total energies were calculated for W defects, *i.e.* SIA configurations and vacancy clusters with up to four vacancies, and for W with hydrogen as an impurity atom, *i.e.* the W surface, SIA and vacancy. For finding the migration barrier of the diffusion process, the minimum energy path between two potential minima was obtained by using the nudged elastic band (NEB) method [51, 52].

As an example of the computing power needed, the maximum computer load was for the H surface penetration calculation using the NEB method: eighteen images each containing $128 + 1$ atoms (six valence electrons per W atom, one electron per H atom) were computed on the Cray XT5 supercomputer's 512 cores (each core having 2.7 GHz and 2 GB of memory).

5 HYDROGEN DIFFUSIVITY

The hydrogen diffusivity in the bulk and on the surface of W were obtained with the harmonic transition state theory combined with DFT calculations. In the next sections, the theory used is outlined and the resulting diffusivities are presented. More detailed results have been presented in Publications **III** and **V**.
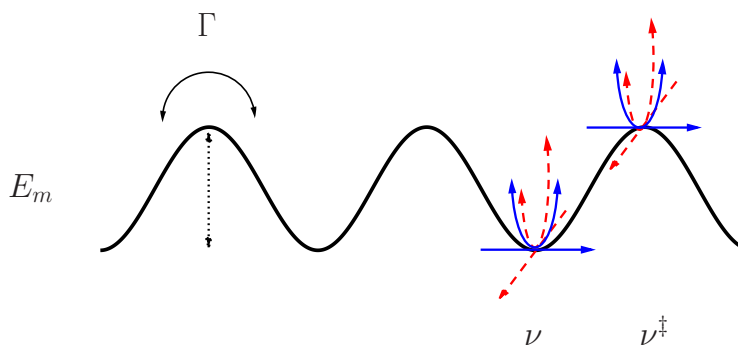
Figure 3: Schematic potential landscape used in the hTST diffusion calculations. The diffusing particle must overcome an energy barrier of height E_m for advancing to a neighbouring ground state. The frequency of the over-barrier jumps Γ is deduced from the harmonic vibrational frequencies, ν and $\nu^{\ddagger}$, at the ground state and on the saddle point, respectively (see Eq. (4)).

5.1 Transition state theory

Statistical mechanics can be used for describing the rate processes of separate atomic reactions. In the reaction process some initial configuration passes through an intermediate configuration, ending up in the final configuration. The intermediate configuration is crucial for the reaction in the sense that once this step is attained the reaction has an extremely high probability to continue to the final configuration. This intermediate phase is called the activated complex [53, 54]. The activated complex is the configuration of the highest potential energy which the system must pass within the reaction process. The reaction rate for the complex is calculated with the partition functions of the system in the initial state and on the activated point [55, 56]. This approach is the constitution of the well-known transition state theory (TST). TST was initially applied for simple reactions, *e.g.* H+H$_2$→H$_2$+H, but interest has been shown in its application for various fields in materials science [57–61].

For diffusion processes, the reaction rate in TST is the jump frequency Γ for the over-barrier motion (Fig. 3). The total partition function of a diffusing particle is $Z = Z_{\text{trans}}Z_{\text{rot}}Z_{\text{vib}}$, where trans, rot and vib refer to the kinetic energy, the moment of inertia and the vibrational energy of the particle, respectively. The jump frequency in TST is $\Gamma = (Z_a/Z)\nu = (Z_a/Z)(p/m^*)$, where Z_a and Z are the total partition functions of the activated state and the ground state, respectively, multiplied by the reactants' average velocity $\nu = (p/m^*)$ per unit length on the activated state [53]. Integrating over momentum p from zero to infinity yields $\Gamma = (kT/h)(Z'_a/Z)e^{-\Delta E/kT}$. The Z'_a is the partition function on the activated state excluding the Z_{trans} since it is present in the $(kT/h)e^{-\Delta E/kT}$ term. ΔE is the energy difference between the activated point and the ground state, and corresponds to the diffusion migration barrier E_m. In the case of diffusion processes the Z_{rot} on the activated point and on the

ground state cancel out. As a result, Γ depends only on Z_{vib}, which can be solved using either the quantum mechanical or the classical solution for harmonic vibrations.

The quantum mechanical solution of the harmonic coscillator yields the harmonic TST (hTST) jump rate

$$\Gamma_{\text{hTST}} = \frac{kT}{h} \cdot \frac{\displaystyle\prod_{i}^{3N-1}\left(\frac{e^{-\frac{h\nu_i^{\ddagger}}{2kT}}}{1-e^{-\frac{h\nu_i^{\ddagger}}{kT}}}\right)}{\displaystyle\prod_{i}^{3N}\left(\frac{e^{-\frac{h\nu_i}{2kT}}}{1-e^{-\frac{h\nu_i}{kT}}}\right)} e^{-\frac{E_m}{kT}} = \frac{kT}{h} \cdot \frac{\displaystyle\prod_{i}^{3N}2\sinh\left(\frac{h\nu_i}{kT}\right)}{\displaystyle\prod_{i}^{3N-1}2\sinh\left(\frac{h\nu_i^{\ddagger}}{kT}\right)} e^{-\frac{E_m}{kT}}, \tag{4}$$

where ν_i and $\nu_i^{\ddagger}$ are the real normal modes of vibration on the ground state and activation state, respectively (Fig. 3), and N is the number of atoms. On the saddle point, there is one real normal mode less than on the ground state, because the negative curvature yields an imaginary frequency, ν^*, in the direction of the reaction coordinate. Simple tunneling probabilities can be examined using ν^* (Publication **III** and references therein).

Using the classical result of the harmonic oscillator, the result of Vineyard [62] is obtained

$$\Gamma_{\text{cl}} = \frac{\displaystyle\prod_{i}^{3N}\nu_i}{\displaystyle\prod_{i}^{3N-1}\nu_i^{\ddagger}} e^{-\frac{E_m}{kT}}. \tag{5}$$

If the frequencies are identical, $\nu_i = \nu_i^{\ddagger} = \nu_0$, the widely used form for the jump frequency is followed $\Gamma_{\text{cl}} = \nu_0 \cdot e^{-E_m/kT}$. It is worth mentioning that the classical result in Eq. (5) is also obtained from Eq. (4) in the high temperature region, *i.e.* when $kT \gg h\nu$. For low temperatures, *i.e.* $kT \ll h\nu$, the quantum mechanical solution, Eq. (4), can be approximated as

$$\Gamma_{\text{hTST}} = \frac{kT}{h} \cdot \frac{\displaystyle\prod_{i}^{3N}(1-e^{-\frac{h\nu_i}{kT}})}{\displaystyle\prod_{i}^{3N-1}(1-e^{-\frac{h\nu_i^{\ddagger}}{kT}})} \exp\left[\left(-E_m - \sum_{i}^{3N-1}\frac{h\nu_i^{\ddagger}}{2} + \sum_{i}^{3N}\frac{h\nu_i}{2}\right)\frac{1}{kT}\right] \tag{6}$$

$$\Rightarrow \Gamma_{\text{hTST}} \approx \frac{kT}{h}\exp\left[-(E_m + \Delta E_{\text{ZPE}})\frac{1}{kT}\right]. \tag{7}$$

It is evident from Eq. (4) that the jump frequency has a temperature-dependent pre-expontial factor not existing in the classical solution. Moreover, Eq. (4) takes into account the zero-point energy

correction for the diffusing particle as $\Delta E_{\text{ZPE}} = \Sigma \frac{1}{2} h \nu^{\ddagger} - \Sigma \frac{1}{2} h \nu$. To obtain the diffusion jump rate with TST, only the migration barrier E_m and the vibrational properties, ν and $\nu^{\ddagger}$, of the diffusing particle at the ground state and on the saddle point need to be determined. As hydrogen is a light mass particle, its vibrational properties are high compared to the metallic host matrix and need to be taken into account. Therefore, Eq. (4) was applied with the DFT calculations of hydrogen diffusivity.

5.2 Interstitial diffusion and diffusion on surfaces

The diffusion rate of atomic interstitials in solid solutions is generally expressed as $D = D_0 \cdot e^{-E_m/kT}$, with D_0 as the diffusion pre-exponential factor. The diffusion rate can be written as $D = \gamma a^2 \Gamma$, where γ is the geometrical factor and a the lattice parameter of the host lattice [63–65]. Γ is the jump rate at which the interstitial jumps to the nearest equilibrium site and is calculated as defined in Sect. 5.1. For tetrahedral interstitial diffusion in a body-centered cubic (bcc) lattice the geometrical factor $\gamma = 1/48$ and the jump length $\lambda = a/\sqrt{8}$ yield

$$D = \frac{1}{6} \lambda^2 \Gamma. \tag{8}$$

The form of Eq. (8) holds for diffusion in primitive cubic lattices [66]. Starting from the well-known one-dimensional definition for diffusion coefficient [67], $D_x = \langle X^2 \rangle / (2t)$, where X is the projected displacement during time t, it can be shown that Eq. (8) is eligible for both interstitial and substitutional diffusion in simple cubic (sc), face-centered cubic (fcc), and bcc lattices.

On the W surface, the adsorbed hydrogen atoms, H_{surf}, are bound to the host atoms with the adsorption energy E_{ads}. The diffusion process is in the plane of the surface and the diffusion rate becomes $D = \frac{1}{4} \lambda^2 \Gamma$. If only one direction, *i.e.* one site, is possible for advancement of diffusion processes, the diffusivity is one-dimensional and the diffusion rate reduces to $D = \frac{1}{2} \lambda^2 \Gamma$.

5.2.1 Diffusion in the bulk

In Fig. 4, the conceivable solution sites for hydrogen in a W bcc lattice are presented. According to the DFT calculations in Publication **III**, the tetrahedral site is the global minimum with an 0.38 eV energy difference to the octahedral site.

Quite different results for the hydrogen diffusivity in W are found in the literature. Experimental results for the migration barrier E_m and the diffusion pre-exponential factor D_0 vary between $0.25 - 1.80$ eV and $3.5 \times 10^{-11} - 6 \times 10^{-4}$ m^2/s, respectively [68–74]. The recommended [75, 76] and widely accepted values are presented in Table 1.
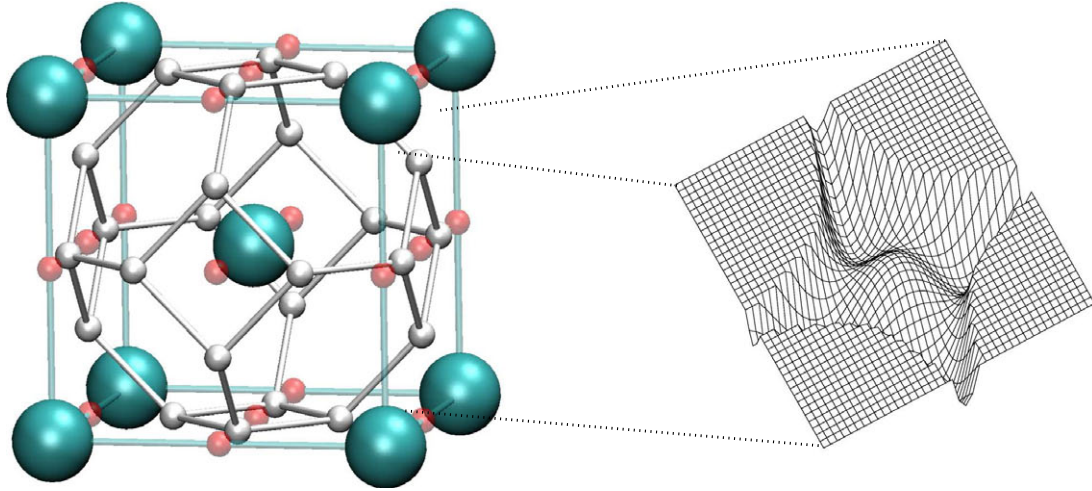
Figure 4: (Left) The bcc lattice with the tetrahedral (white) and octahedral (red) sites for H interstitial solution. Only atoms in the unit cell are shown. (Right) The potential landscape viewed on the bcc [100] plane. The octahedral site in the middle surrounded by four tetrahedral sites is a metastable state with negative curvature into two directions. The adjacent tetrahedral sites are separated by a potential barrier of height E_m. For visualization, the barrier heights extending over the octahedral barrier height have been cut out near the locations of the host atoms.

In this work the E_m for the diffusion of H in W was calculated with the NEB method. The jump rate Γ_{hTST} was deduced from the DFT frequency calculations at the ground state ν, and at the saddle point $\nu^\ddagger$. Frequencies were obtained by displacing the vibrating atom in the direction of each cartesian coordinate and calculating the second derivative of the energy. In Publication **III** it was shown, that the Γ_{hTST} for H, D and T has the classical isotope effect $(1/\sqrt{m})$ at temperatures $\gtrsim$ 200 K.

The resulting E_m for the hydrogen diffusion in W is 0.21 eV. The values for ν and $\nu^\ddagger$ are presented in Publication **III**. The resulting D is illustrated in Fig. 5 and compared with the experimental values in the literature [70, 71, 74]. The DFT results agree with the Arrhenius fit to the experimental data

Table 1: Hydrogen diffusivity in W obtained with DFT calculations compared to the experimental results: enthalpy of solution S, diffusion barrier E_m and diffusion pre-exponential factor D_0. From Publications **III** and **V**.

H in bcc W	Experimental [a]	This work
S (eV)	1.04	0.95
E_m (eV)	0.39, 0.25 [b]	0.21, 0.26 [c]
D_0 (m^2/s)	4.1×10^{-7}, 1.6×10^{-7} [b]	5.2×10^{-8}, 4.8×10^{-8} [c]

[a]Ref. [70]. Experimental diffusivity for temperatures > 1100 K.
[b]Arrhenius fit to expt. data at temperatures > 1500 K from Ref. [70].
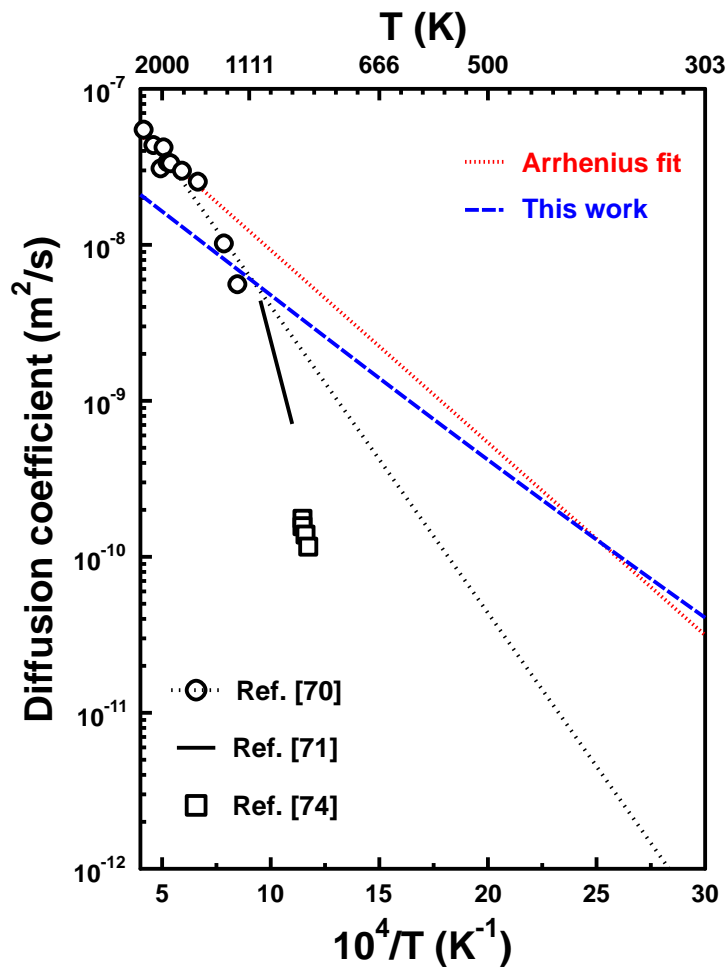[c]Unrelaxed W atoms along the diffusion path.

Figure 5: The H diffusivity in bulk W obtained with DFT according to TST (blue line, $E_m = 0.21$ eV). The results agree with the Arrhenius fit to the experimental data above 1500 K (red line, $E_m^{\text{fit}} = 0.25$ eV). The experimentally found hydrogen diffusion is influenced by trapping up to 1500 K [74, 75]. From Publication **III**.

points above 1500 K ($E_m^{\text{fit}} = 0.25$ eV). As suggested in [74, 75] and discussed in Publication **III**, H diffusion in W is strongly influenced by trapping effects up to 1500 K, which is corroborated with these DFT calculations. Moreover, positron annihilation spectroscopy (PAS) experiments on clean W have shown that vacancy clusters with up to $40 - 60$ vacancies, that are ideal for hydrogen trapping, can still be present in the lattice at $1500 - 1650$ K [77].

The NEB method gives the saddle point energy of the true minimum path between two adjacent ground states. On the saddle point the three nearest-neighbor W atoms were found to be displaced by 0.045, 0.042 and 0.002 Å from the ideal lattice site during the hydrogen over-barrier motion. Since the diffusing H atom has a high vibrational frequency compared with surrounding metal atoms, it is questionable whether the W atoms have time to find their relaxed lattice sites during the rapid hydrogen diffusion. A NEB calculation allowing *no* relaxation of the W atoms on the reaction path

results in $E_m = 0.26$ eV, which is found to be in perfect agreement with the experimental barrier obtained from the slope of the Arrhenius fit. This leads to the conclusion that the over-barrier diffusion of hydrogen in metals is extremely rapid and the considerably heavy host matrix atoms have no time to move aside during the hydrogen diffusion process.

5.2.2 Surface diffusion

The tungsten surface has been under extensive research for decades [78]. Several experimental studies [35, 36, 79–87] are accompanied by computational methods [88–91] for the study of hydrogen chemisorption on tungsten.

In this work the surface diffusion of hydrogen on tungsten was examined on a (100) surface. The clean $W(100)$ surface has been studied extensively and the reconstruction mechanism is well reported [81–83, 86]. The DFT calculations reproduced the reconstructed morphology accurately and the explanatory results are presented in Publication **V**.

The hydrogen coverage phase β_2 on a $W(100)$ surface was studied. Two adsorption sites with different E_{ads} were identified. From the energetics of the surface sites (Fig. 6) it can be concluded that the hydrogen surface diffusion proceeds via the short bridge sites *i.e.* the diffusion rate used is $D = \frac{1}{2}\lambda^2\Gamma$. This is confirmed since the DFT calculated migration barrier (0.43 eV) and the diffusion pre-exponential factor (0.5×10^{-6} m^2/s) agree with the experimentally known diffusion values of 0.47 eV and 1.2×10^{-6} m^2/s, respectively [92]. Using the assumption of unrelaxed W atoms on the saddle point, as presented in Sect. 5.2.1, yields $E_m = 0.46$ eV which is in perfect agreement with the experimental value.

Table 2: Hydrogen diffusivity on W(100) surface obtained from DFT calculations compared to the experiments: diffusion barrier E_m and diffusion pre-exponential factor D_0. From Publication **V**.

H on W(100)	Experimental [a]	This work
E_m (eV)	0.47	0.43, 0.45 [b]
D_0 (m^2/s)	1.2×10^{-6}	0.5×10^{-6}, 0.5×10^{-6} [b]

[a] Ref. [92]. Experimental diffusivity for 220 K $< T <$ 310 K.
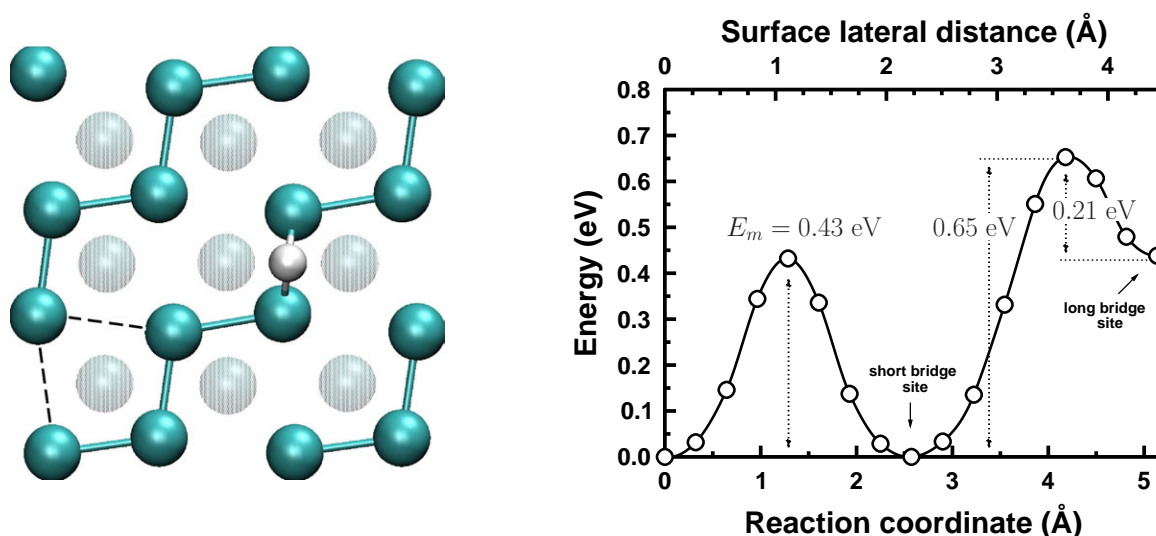[b] Unrelaxed W atoms along the diffusion path.

Figure 6: (Left) The reconstructed W(100) surface with H atom on the short bridge site. Dashed lines are the long bridge sites. (Right) Potential barriers between the hydrogen adsorption sites on W(100) surface obtained with NEB calculations. From Publication **V**.
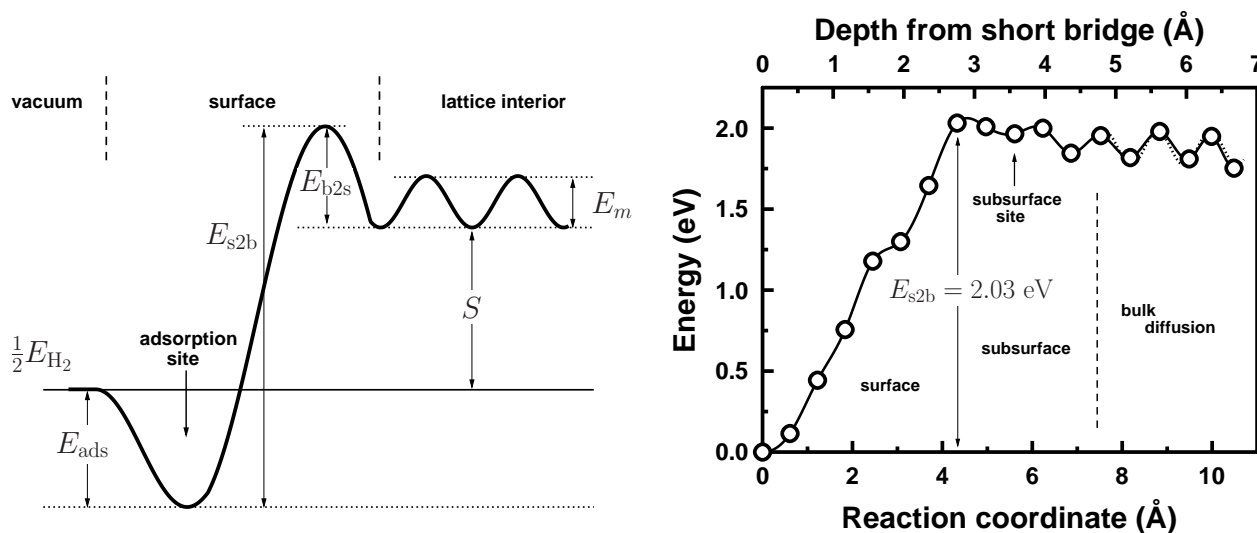

Figure 7: (Left) Schematic potential landscape from the surface to the bulk as a function of depth. The ad-atom is bound to the surface with an adsorption energy E_{ads}. In order to jump from the surface to the solute site with energy S, the particle must overcome the surface-to-bulk barrier E_{s2b}. For the bulk-to-surface migration an energy of E_{b2s} is needed. (Right) The calculated migration energetics of hydrogen from the W(100) surface to the solute site in the bulk. The bulk-like diffusion via neighboring tetrahedral sites is present at depths beyond ~ 4.5 Å. From publication **V**.

5.2.3 Migration from surface to the bulk

The hydrogen dissociation path from the $W(100)$ surface short bridge site to the solute site in the bulk was calculated using the NEB method. The main results are given in Publication **V**. The resulting energy diagram is represented in Fig. 7. The high energy needed for the hydrogen migration from the surface to the solute site in the bulk (~ 2 eV) and the low barrier for reversible migration (~ 0.27 eV) indicate that hydrogen is easily agglomerated at the surface.

Moreover, the surface-to-bulk energetics can be associated, *e.g.*, with hydrogen detrapping from large surface areas in the bulk. The adsorption sites inside grain boundaries, voids or large bubbles can be very similar to those at the surface.

6 TRAPPING OF HYDROGEN TO POINT DEFECTS AND EXTENDED DEFECTS

In the following sections, the results of hydrogen trapping defect concentration profiles in W, as obtained both experimentally and computationally, are presented. The hydrogen trapping energies of each trap type are compared with the experimental results. The experimental results are presented in Publications **I** and **II** and the detrapping energies with corresponding release temperatures are from Publications **V** and **VI**. The theoretical cascade results are based on the clustering results presented in Publication **IV**.

6.1 Experimental results

The concentration profiles of the retained D obtained with SIMS and normalized with NRA are presented in Fig. 8. From the profiles it is evident that higher implantation energies move the D concentration maximum deeper in the samples and that more implantation-induced damage is produced. Since hydrogen has a high diffusivity in W and it is mobile at room temperature, the concentration profiles obtained represent the hydrogen trapping defect profiles. This is confirmed by the fact that by comparing the as-implanted projected ranges of $R'_p \sim 15$, 38 and 100 nm with projected ranges $R_p \sim 36$, 86 and 155 nm obtained with binary collision calculations for the energies 5, 15 and 30 keV, respectively, it is evident that the implanted D does not halt in the implanted region, but diffuses rapidly away from it and gets trapped into the implantation-induced damage. In Publication **I** it was shown that the as-implanted D profiles can be assigned with the implantation-induced vacancy profiles in the samples.
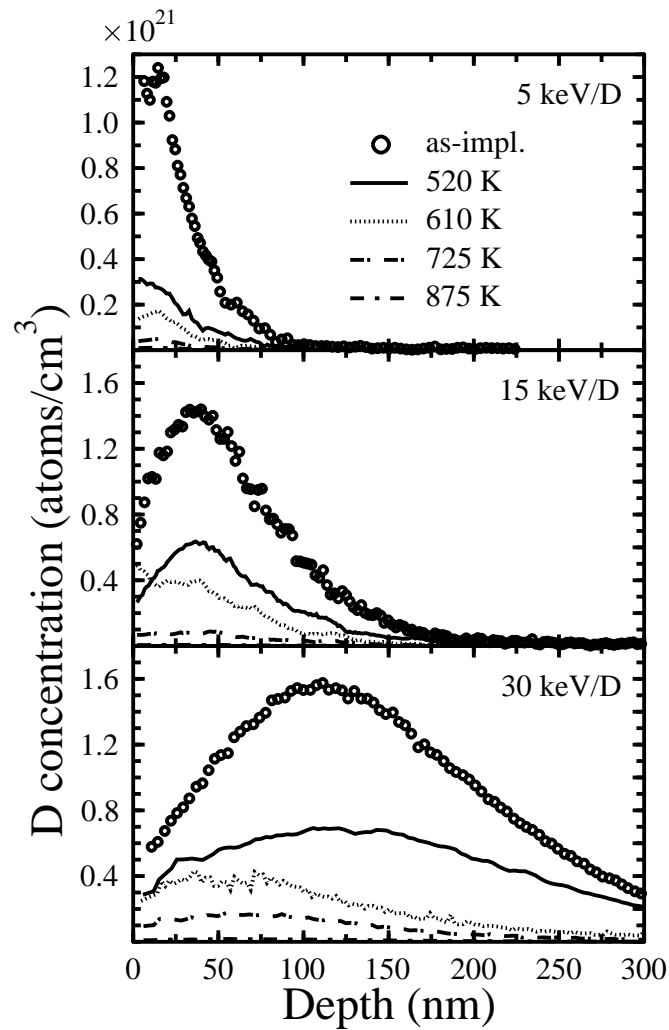
Figure 8: The retained D concentration profiles of 5, 15 and 30 keV implantations obtained with SIMS and normalized with NRA. Annealing of the samples at the pre-determined temperature emptied the corresponding trap from D and unmasked the underlying trap profile. From Publication **II**.

The concentration analyzes of the as-implanted samples show the profile of the total amount of the D retained in the sample. Part of D can be considered to be trapped in the grain boundaries and dislocations, which can be seen in the D profile tail extending deeper into the bulk. Recent SIMS and NRA analyzes on retained D concentrations in W have shown this tail extending even up to depths of > 7 μm [93, 94].

The subsequent annealings revealed the variation in the defect profiles. The difference in the areal concentrations of the profiles can be associated with the total amount of desorbed D_2 measured with TDS in the course of annealing. The nature of these trap types are discussed in Sect. 6.2.
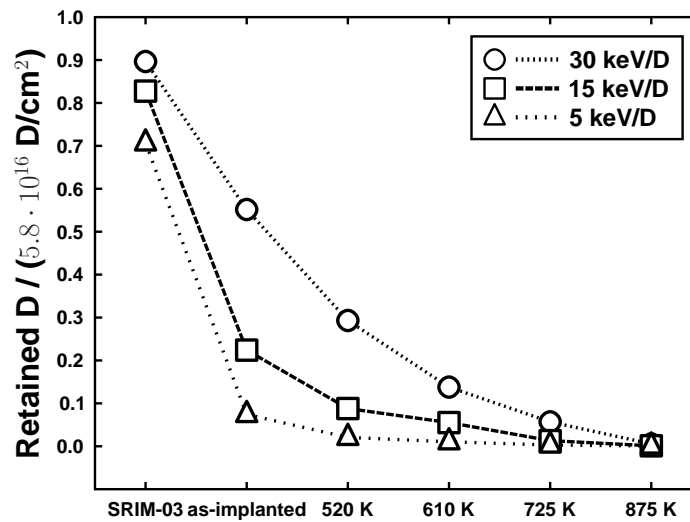
Figure 9: The retained amount of implanted D in W as a function of the annealing temperature measured with the NRA. Results from the binary collision calculations (incl. backscattering) are shown as a reference to the as-implanted concentrations. From Publication **II**.

The concentration of traps decreases with implantation energy. In Fig. 9, the trap count generated in the course of implantation is presented. With decreasing implantation energy, the total amount of retained D decreased from 55% to 22% and further to 7%. From binary collision calculations it was found that the fraction of reflected D atoms increases from 10% to 17% and further to 29% with decreasing implantation energy.

6.2 Theoretical results

6.2.1 Detrapping from intrinsic defects

Hydrogen atoms are easily immobilized by defects in the material. Self-trapping is precluded because of the strong repulsion between nearby hydrogen atoms in solid W [13, 14] (Publication **III**). H_2 molecules are formed in vacuum or in other commensurable conditions. Besides the solute hydrogen atoms, the repulsion is effectively seen with the hydrogen in the W monovacancy (V_1). In Fig. 10 are presented two H atoms at their lowest energy state. This is due to the breaking of H_2 and the bonding of H with its nearest W neighbor outside the vacancy.

TDS measurements are widely used for determining the detrapping energetics experimentally [37, 77, 95–98]. The particle dissociation from a trap is affected by the sample temperature used and by the vibrational properties of the particle in the trap. By increasing the sample temperature linearly with a heating rate δ, trapped atoms are dissociated from the defect type i, and $E_{\text{trap},i}$ corresponds to the
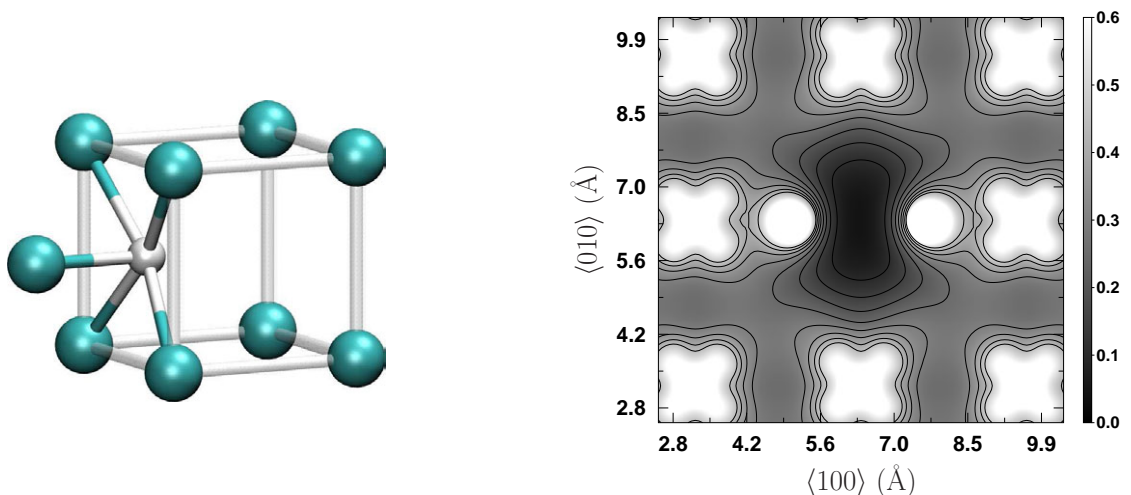
Figure 10: Hydrogen in the W monovacancy. (Left) H atom in its ground state at the distorted octahedral site. H is bound to its nearest neighbour outside the vacancy and to the four second nearest W atoms. (Right) The charge densities ($e/\text{Å}^3$) of two H atoms at their ground states in a W vacancy. There is no bonding between the two hydrogens. From Publication **VI**.

release temperature T_m as [99]

$$\frac{E_{\text{trap},i}}{kT_m^2} = \frac{\nu_i}{\delta} \exp\left(-\frac{E_{\text{trap},i}}{kT_m}\right). \tag{9}$$

Besides the energy needed to detrap, $E_{\text{trap},i}$, also the particle's escape attempt frequency ν_i can be obtained from DFT calculations.

The TDS heating curves of the W samples for emptying each trap type sequentially are presented in Publications **I** and **II**. Approximative δ values can be obtained from these curves and the results for hydrogen trapping energies to point defects are presented in Publication **VI**. With the use of Eq. (9), and taking into account the DFT-calculated $E_{\text{trap},i}$ and ν_i values for H, the following conclusions can be drawn:

– In the course of emptying the first trap type, the TDS signal reached its maximum at $T_{\text{TDS}} \sim 510$ K, which corresponds to the release of hydrogen atoms with $E_{\text{trap}} < 1.4$ eV ($T_m \sim 490$ K).

– The second trap type with $T_{\text{TDS}} \sim 600$ K is needed for completely emptying the vacancies with $E_{\text{trap}} \approx 1.6$ eV ($T_m \sim 590$ K).

– The third trap type with a TDS temperature of ~ 720 K is related to vacancy migration and is discussed in Sect. 6.3.

– The fourth trap with $T_{\text{TDS}} \sim 820$ K is associated with hydrogen release from large surface areas, *e.g.* vacancy clusters, with $E_{\text{trap}} > 2$ eV ($T_m > 750$ K).
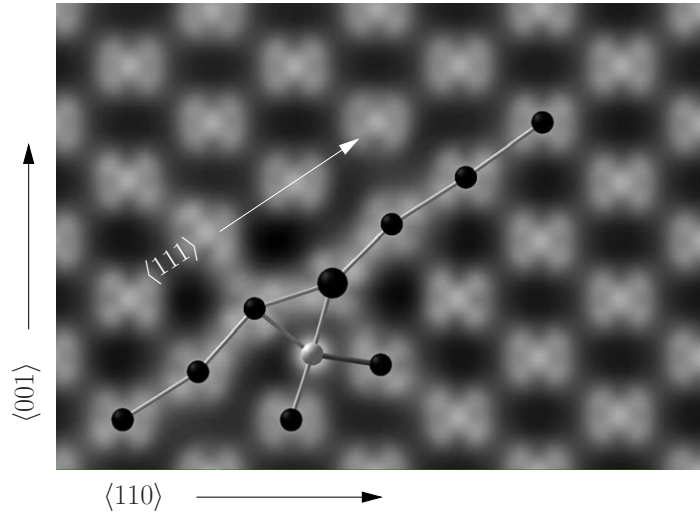
Figure 11: The distortion of the ⟨111⟩ SIA quasiparticle produced by hydrogen (light colored atom). From Publication **VI**.

The self-interstitial atom (SIA) is not an effective trapping site for H, since the DFT-calculated detrapping temperature is <RT. However, the SIA is a quasiparticle by nature [100] extending over three displaced W atoms in the forward and backward ⟨111⟩ directions, and the presence of H induces distortion in the quasiparticle geometry (Fig. 11). The distortion can further enhance the formation of dislocations, which in turn trap hydrogen above room temperature [101].

As transmutation of W atoms to Re and further to Os occurs, an increase in the hydrogen inventory in bulk W can take place. The substitutional Re and Os were not found to trap hydrogen which is consistent with the experimental results [6]. However, the interstitial Os turned out to be a hydrogen trapping defect with $E_{\mathrm{trap}} \sim 1$ eV (Publication **VI**).

6.2.2 Deuterium concentration profiles

The combination of different computational methods form the foundation of multiscale modelling, which has become feasible in the past decade due to the increase of computational resources. An illustrative example of multiscale modelling is the study of the recovery stages of irradiated iron by combining DFT and Monte Carlo calculations [102].

The D-implantation-induced collision cascades and the subsequent trap profiles in annealed W were studied with the developed BOP parameter set in combination with binary collision and rate theory calculations. The results from the 5, 15, and 30 keV/D implantation cascade analyses are shown in Fig. 12. In the beginning of the analyses, the initial vacancy damage profile and the recoil energies in the damage cascades were obtained from the binary collision calculations carried out with the SRIM
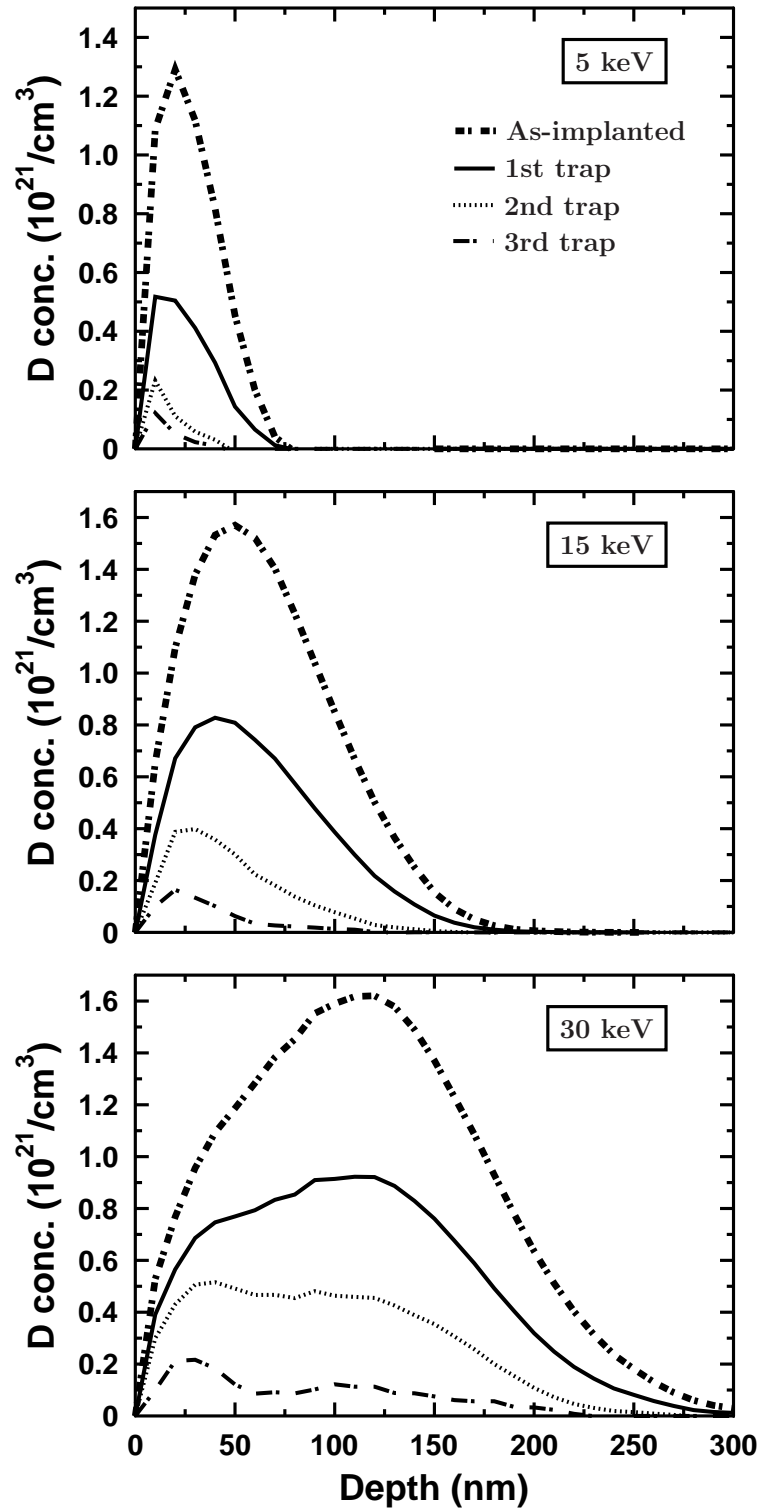
Figure 12: The computational profiles of the retained deuterium after 5, 15, and 30 keV/D implantations into W. The 1st, 2nd, and 3rd trap correspond to the experimental TDS temperatures of 520, 610, and 725 K, respectively.
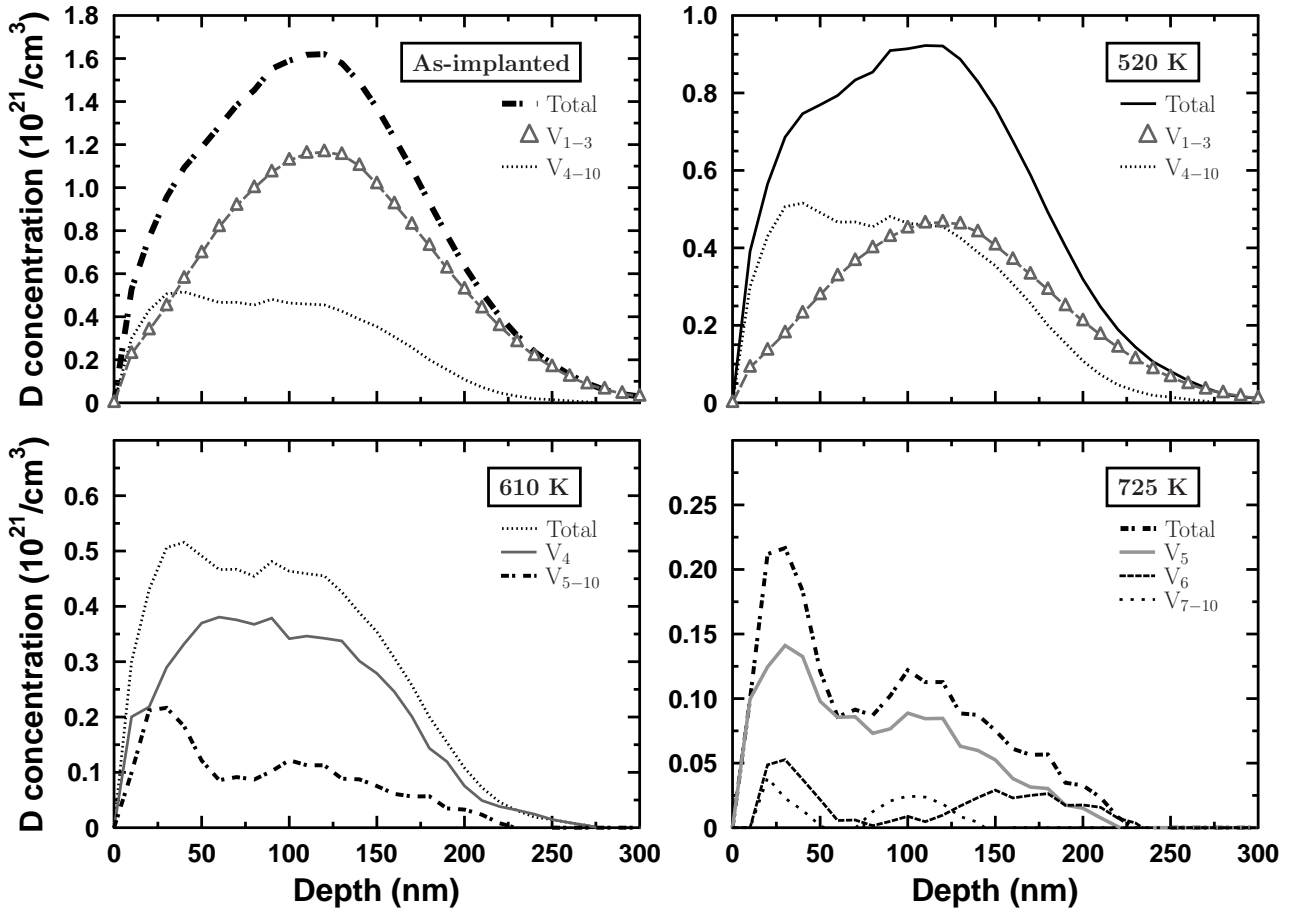
Figure 13: The computational deuterium profiles of 30 keV/D^+ implantation into W. Temperatures 520, 610, and 725 K refer to the 1st, 2nd, and 3rd trap, respectively. The total concentration at each trap is composed of D distributed into vacancy clusters of $V_1 - V_{10}$.

software [33]. The initial SIA distribution was deduced from the recoil energy information as well as the W damage obtained from the MD simulations using the developed W potential [103]. The Frenkel pair recombination radius for polycrystalline W was taken as $R_{\text{Frenkel}} \approx 8.07$ Å, which is the radius of a spherical volume equal to the Frenkel pair ellipsoidal volume in single-crystal W presented in Publication **IV**. The vacancy clustering radii, R_{T}^{v}, were taken from the same Publication as $R_{\text{T}}^{v} = (4.4 + 0.2 \cdot N_v)$Å, where N_v is the number of vacancies in the cluster. Systems up to $N_v = 10$ (V_{10}) were studied. In other words, the various radii were used to study the *immediate* annihilation and clustering processes in the material. In the beginning of the analysis, the correlated annihilation and clustering within each cluster was examined, *i.e.* the Frenkel pair annihilation and the formation of V_{1-10} clusters. Finally, all the *un*correlated Frenkel pair annihilations, SIA clustering and vacancy clustering events were studied. As a result, $\sim 99\%$ of the vacancy damage comprises of V_{1-3}'s of which over 90% are monovacancies. An equal amount of SIAs are formed, which have been shown to be extremely mobile in W (Publication **IV** and Refs. [104–112]). Since the cascade analysis performed features no time dependence, the mobilities of the SIAs as well as the consequent annihilation with vacancies or ending up to the surface, were studied with rate theory calculations [113]. As a result, $\sim 95\%$ of the V_{1-3} were annihilated with the SIAs. This reproduced well the experimental D concentration profiles as will be shown next.

The D concentrations in the vacancy clusters were determined with the results presented in Publication **VI** and summarized in Sect. 6.2.1. It was shown that the W monovacancy can be populated with five hydrogen atoms at room temperature. The D concentration in V_1 was extrapolated proportionally into larger vacancy entities, *i.e.* the maximum D concentration in a divacancy is twice that for the V_1, and so forth. As a result, the retained D concentration profiles have been reproduced (Fig. 12) and were found to be in good agreement with the experimental ones (Fig. 8). The D release from vacancies takes place with respect to the corresponding E_{trap}, leading to consecutive detrapping instead of simultaneous release. The concentration maxima are located at the same depths as in the experiments, and the damage profiles are found to shift towards the surface. However, a more detailed computational analysis can be obtained by taking into account the implantation dynamics by using methods that allow processes in large time scales. An example of such a method is the use of the rate theory involving also the mobile hydrogen [113].

From the computational profiles, detailed analysis of the nature of different traps can be made. The D concentrations retained in various vacancy clusters after 30 keV/D implantation are presented in Fig. 13. Most of the D is trapped in V_1, which is also reasonable due to the high migration energy needed for vacancy diffusion in W and in other metals. However, large vacancy clusters are formed closer to the surface. The number and size of these clusters increase as higher implantation fluences

are used. This can lead to formation of voids and other microcavities that can efficiently trap hydrogen. The hydrogen blistering phenomenon cannot be explained by the formation of these large cavities close to the surface, since the experimentally observed blister lid thicknesses are several orders larger than the R_p of the hydrogen projectiles. However, the void formation increases stress in the bulk which in turn can enhance the blister formation. According to the theory of blister formation [28], the mismatch in the depth concentrations of the implanted species (hydrogen) and defect distribution (vacancies, voids, *etc.*) ignites a stress peak far beyond the implantation zone, which can lead to the blister formation. The high diffusivity of free SIAs can produce interstitial clusters and dislocation loops deeper in the bulk. These large scale defects can further trap mobile hydrogen and give rise to the hydrogen inventory beyond the implanted region.

6.3 Summary of the hydrogen retention properties

For determining the hydrogen retention and re-emission in materials, numerous parameters for describing the defect properties, evolution of defects and the quality of the hydrogen-defect interactions are needed. These can be obtained both experimentally and computationally, once the foundation of the setup or model used is well established. In the following, the obtained hydrogen interactions in the bulk crystalline W are summarized (Table 3), taking into account the structural evolution of the metallic host matrix above RT.

Hydrogen implantations at RT yield damage profiles in W with the following characteristics. The amount of damage increases with the implantation energy and the damage profiles move further into the bulk. The majority of the damage consists of point defects albeit some defect clusters are formed between the surface and the damage profile maximum. The amount and size of the clusters increase with the implantation fluence and energy.

Four different types of traps were identified with TDS, and the retained hydrogen concentration at each trap was deduced with NRA and SIMS (Fig. 8). The maximum TDS temperature for emptying the first trap was $T_{\text{TDS}} \approx 510$ K. According to the DFT results in Publication **VI**, this can be connected to the dissociation of the loosely bound $3^{\text{rd}} - 5^{\text{th}}$ hydrogen from the monovacancy. Experimentally it has been observed that hydrogen release from dislocation loops also starts in this temperature range [101]. Since hydrogen was found to have a strong repulsion towards other hydrogen atoms even inside the monovacancy, it can be argued that also divacancy and trivacancy with small open volumes have similar H trapping energies as the monovacancy.

The second trap type was emptied with a maximum TDS temperature of 610 K. The PAS experiments [37, 77] have shown that this peak is connected to the D dissociation from the V_1 with an energy of

~ 1.43 eV. According to the present DFT calculations (Publication **VI**), this peak is coupled to the simultaneous detrapping of the 1$^{\text{st}}$ and 2$^{\text{nd}}$ hydrogen from the V$_{1-3}$'s which will then be completely unoccupied by hydrogen. The DFT-approximated release temperature was < 600 K.

The TDS maximum temperature of 725 K for emptying the third type of trap can be attributed with the structural change of W during the V$_1 \rightarrow$ V$_{4-10}$ clustering. Pristine W goes through major structural evolution with increasing temperature. The V$_1$'s start to migrate at ~ 650 K and form small size clusters of V$_{4-10}$ according to the PAS experiments [77]. The reported V$_1$ migration temperature corresponds to the energy of $E_m^v = 1.70$ eV calculated in Publication **IV**. This agrees with the experimental value of 1.78 eV. Moreover, at this temperature region the empty V$_{2-3}$ can increase the number of diffusing V$_1$'s, since their dissociation energies have been found to be 1.72 and 1.90 eV, respectively [103].

The maximum temperature needed to empty the fourth trap type was 875 K. No major structural evolution of the W host matrix is present at $750 - 1000$ K, *i.e.* the PAS studies have shown the V$_{4-10}$ clusters to be immobile at this temperature [77]. This is coherent with the DFT result that the V$_4$ dissociation energy is 2.5 eV [103]. Therefore, the fourth TDS peak observed is associated with hydrogen release from the inner surface of these large vacancy clusters or other microcavities. The hydrogen detrapping energies from these defects are taken to be $\gtrsim 2$ eV according to the surface calculations presented in Publication **V** (Fig. 7).

As a final remark, hydrogen implanted with low energies and low fluences are retained in mono-vacancies which are completely emptied at ~ 600 K. With higher fluences the number and size of vacancy clusters and voids increase. These defects store hydrogen in substantial amounts and higher detrapping energies, *i.e.* higher release temperatures, are needed.

Table 3: Summary of the hydrogen detrapping temperatures above room temperature, the corresponding recovery stages of bulk W and the dissociation energies obtained with the DFT calculations.

Temperatures used in TDS for emptying a trap (from Publications **I** & **II**)	Reported hydrogen TDS peak temperatures	Structural evolution of bulk W analyzed with PAS [a]	Energetics obtained with DFT (from Publication **VI**)
RT $\rightarrow$ 520 K	403 K [b], 450 K: dislocation loops [c], 500 K: low energy natural traps [d]		dissociation from SIAs and $H_N V_1$, $N = 3-5$ with $E_{trap} \lesssim 1.4$ eV
520 K $\rightarrow$ 610 K	573 K [b], 550 K: dissociation of $D_1 V_1$ with 1.43 eV [a], $H_1 V_1$ with 1.55 eV [e]		dissociation of $H_N V_1$, $N = 1, 2$ with $E_{trap} \sim 1.6$ eV
610 K $\rightarrow$ 725 K	673 K [b],	600 $-$ 750 K: clustering of $V_1 \rightarrow V_{4-10}$	V_1 migration energy 1.7 eV, dissociation of V_2 and V_3.
725 K $\rightarrow$ 875 K	803 K [b], 800 K: D desorption from V_{11-16} [a]	750 $-$ 900 K: V_{4-10}'s stable	V_{4-10}'s bound with $E_b \gtrsim 2.5$ eV [103], desorption of H from cavities, $E_{s2b} \gtrsim 2$ eV (Publication **V**)
875 K $\rightarrow$ 1000 K	998 K [b]	900 $-$ 1150 K: clustering of $V_{4-10} \rightarrow V_{11-16}$	
		1350 $-$ 1500 K: clustering of $V_{11-16} \rightarrow V_{40-60}$	
		> 1700K: no defects	

[a] 30 keV/D and 15 keV/D in single crystal W(100), Refs. [37, 77], respectively.
[b] 500 eV/D in various forms of W, Ref. [96].
[c] 5 keV/D in single crystal W(111), Ref. [101].
[d] 0.1, 1.5 and 8 keV/D in single crystal and wrought W, Ref. [73].
[e] PAC, Ref. [114].

7   CONCLUSIONS

Tungsten has been chosen to be used as the plasma-facing divertor material in the next step fusion device ITER. Therefore studies on the interactions of W with hydrogen originating from the fusion plasma are of significant importance. In this thesis, results for hydrogen migration and retention properties in tungsten, as obtained with experimental ion beam methods and state of the art computational methods, are presented.

Implantations were carried out with varying energies to study the retained hydrogen profiles. The retained concentrations were determined by using a novel method that combines the quantitative accuracy of NRA with the good depth resolution of SIMS. The retention was found to decrease rapidly with the implantation energy. One of the reasons that led to the decreased retention is the increased backscattering effect with decreasing energy, but the main reason is the reduced damage produced per implanted hydrogen.

The subsequent annealings of the W samples and *in situ* TDS measurements revealed the existence of four hydrogen trapping defect types with release temperatures ranging from room temperature to 900 K. The defect profiles with higher release temperatures, *i.e.* detrapping energies, were formed closer to the sample surface.

Multiscale computational methods were employed for conducting cascade analyses of the implantation profiles. Based on DFT calculations presented in this thesis, a parameter set for a bond-order potential energy function for MD simulations for describing the W defect properties was developed. With the aid of the potential, numerical values for describing the defect annihilation and clustering processes in the bulk were determined. These were used as input in the cascade analysis of the results from binary collision calculations. The dynamics of the rapidly migrating SIAs were solved with rate theory calculations, leading to a substantial decrease of point defects.

The computational results were successfully compared with the experiments, revealing the nature of the experimentally observed traps. The majority of the implantation induced damage composed of monovacancies, whereas the damage profiles near the surface consist of clustered defects. A direct application of the damage analysis for ITER-relevant conditions is the analysis of the cascade profiles in tungsten induced by the high neutron flux from the fusion reactions in the plasma.

Many experimental and computational analyses within the fusion community need the parameters of hydrogen diffusivities in various metals as an input. In this thesis, the energetics and diffusivity of hydrogen in tungsten were obtained using DFT calculations and transition state theory. As a result, adjusted values for the diffusivity in W have been presented. The diffusion of hydrogen is rapid in

metallic matrices, partly due to the high vibrational frequency of the low-mass hydrogen compared to the surrounding heavy metal atoms. The metal atoms have no time to move during the over-barrier motion of hydrogen. The obtained hydrogen diffusivity values were extensively validated and compared with the commonly referred experimental results. The presented diffusion pre-exponential factor and the migration barrier are proposed to be taken into consideration in the future code development for the trapping and detrapping studies of hydrogen in tungsten.

The aforementioned conclusions have been drawn from detailed analyses of the hydrogen-implantation-induced damage profiles in tungsten and from the state-of-the-art computer calculations of the hydrogen energetics. The results obtained have shown the value and the essence of the growing need for combined experimental analyses and computational methods to describe microscopic effects in materials science.

ACKNOWLEDGMENTS

References

1. Information on fusion tehcnology, history and development can be found on the ITER web page, http://www.iter.org .

2. ITER Physics Basis Editors, ITER Physics Expert Group Chairs and Co-Chairs and ITER Joint Central Team and Physics Integration Unit, *ITER Physics basis*, Nuclear Fusion **39**, 2137 (1999).

3. H. Bolt, V. Barabash, G. Federici, J. Linke, A. Loarte, J. Roth, and K. Sato, *Plasma facing and high heat flux materials - needs for ITER and beyond*, J. Nucl. Mater. **307-311**, 43 (2002).

4. *ITER Documentation 2001*, ITER Technical Basis G A0 FDR 1 01-07-31 R1.0 .

5. G. Federici, C. Skinner, J. Brooks, J. Coad, C. Grisolia, A. Haasz, A. Hassanein, V. Philipps, C. Pitcher, J. Roth, W. Wampler, and D. Whyte, *Plasma-material interactions in current tokamaks and their implications for next step fusion reactors*, Nucl. Fusion. **41**, 1967 (2001).

6. A. Golubeva, M. Mayer, J. Roth, V. Kurnaev, and O. Ogorodnikova, *Deuterium retention in rhenium-doped tungsten*, J. Nucl. Mater. **363-365**, 893 (2007).

7. J. Roth, E. Tsitrone, T. Loarer, V. Philipps, S. Brezinsek, A. Loarte, G. F. Counsell, R. P. Doerner, K. Schmid, O. V. Ogorodnikova, and R. A. Causey, *Tritium inventory in ITER plasma-facing materials and tritium removal procedures*, Plasma Phys. Control. Fusion **50**, 103001 (2008).

8. W. Eckstein and J. P. Biersack, *Reflection of low-energy hydrogen from solids*, Appl. Phys. A **38**, 123 (1985).

9. *Hydrogen Recycling at Plasma Facing Materials.* NATO Science Series II, Mathematics, Physics and Chemistry, Vol. 1, edited by C. H. Wu (Kluwer Academic Publishers, Dordrecht, Netherlands, 2000).

10. *Ion implantation techniques*, 1st ed., edited by H. Ryssel and H. Glawischnig (Springer-Verlag, Berlin, Heidelberg, New York, 1982).

11. C. S. Becquart and C. Domain, *Migration Energy of He in W Revisited by Ab Initio Calculations*, Phys. Rev. Lett. **97**, 196402 (2006).

12. J. K. Nørskov, *Electron structure of single and interacting hydrogen impurities in free-electron-like metals*, Phys. Rev. B **20**, 446 (1979).

13. K. O. E. Henriksson, K. Nordlund, A. Krasheninnikov, and J. Keinonen, *Difference in formation of hydrogen and helium clusters in tungsten*, Appl. Phys. Lett. **87**, 163113 (2005).

14. C. Becquart and C. Domain, *A density functional theory assessment of the clustering behaviour of He and H in tungsten*, J. Nucl. Mater. **386-388**, 109 (2009).

15. N. Baluc, *Assessment Report on W*, Final Report on EFDA Task TW1-TTMA-002 (2002).

16. G. Cottrell, *Sigma phase formation in irradiated tungsten, tantalum and molybdenum in a fusion power plant*, J. Nucl. Mater. **334**, 166 (2004).

17. R. Pampin, *Tungsten transmutation and resonance self-shielding in PPCS models for the study of sigma-phase formation*, UKAEA FUS 525, EURATOM/UKAEA Fusion (2005).

18. Y. Nemoto, A. Hasegawa, M. Satou, and K. Abe, *Microstructural development of neutron irradiated W-Re alloys*, J. Nucl. Mater. **283-287**, 1144 (2000).

19. J. He, A. Hasegawa, and K. Abe, *Effects of transmutation elements on the defect structure development of W irradiated by protons and neutrons*, J. Nucl. Mater. **377**, 348 (2008).

20. *Sputtering by Particle Bombardment I. Physical sputtering of single element solids*, 1st ed., edited by R. Behrisch (Springer-Verlag, Berlin, Heidelberg, New York, 1981).

21. *Sputtering by Particle Bombardment: experiments and computer calculations from threshold to MeV energies*, edited by R. Behrisch and W. Eckstein (Springer, Berlin, Heidelberg, 2007).

22. A. Kirschner, P. Wienhold, V. Philipps, J. P. Coad, A. Huber, and U. Samm, *Modelling of carbon transport in fusion devices: evidence of enhanced re-erosion of in-situ re-deposited carbon*, J. Nucl. Mater. **328**, 62 (2004).

23. K. Heinola, T. Ahlgren, W. Rydman, J. Likonen, L. Khriachtchev, J. Keinonen, and C. H. Wu, *Effect of Hydrogen on Flaking of Carbon Films on Mo and W*, Phys. Scripta **T108**, 63 (2004).

24. C. H. Wu and U. Mszanowski, *A comparison of lifetimes of beryllium, carbon, molybdenum and tungsten as divertor armour materials*, J. Nucl. Mater. **218**, 293 (1995).

25. A. Kukushkin, H. Pacher, V. Kotov, D. Reiter, D. Coster, and G. Pacher, *Effect of neutral transport on ITER divertor performance*, Nucl. Fusion. **45**, 608 (2005).

26. *Sputtering by Particle Bombardment II. Sputtering of alloys and compounds, electron and neutron sputtering, surface topography*, 1st ed., edited by R. Behrisch (Springer-Verlag, Berlin, Heidelberg, New York, 1983).

27. W. Wang, J. Roth, S. Lindig, and C. H. Wu, *Blister formation of tungsten due to ion bombardment*, J. Nucl. Mater. **299**, 124 (2001).

28. Y. V. Martynenko, *The theory of blister formation*, Radiat. Eff. Defect S. **45**, 93 (1979).

29. V. K. Alimov, J. Roth, R. A. Causey, D. A. Komarov, C. Linsmeier, A. Wiltner, F. Kost, and S. Lindig, *Deuterium retention in tungsten exposed to low-energy, high-flux clean and carbon-seeded deuterium plasmas*, J. Nucl. Mater. **375**, 192 (2008).

30. A. A. Haasz, M. Poon, and J. W. Davis, *The effect of ion damage on deuterium trapping in tungsten*, J. Nucl. Mater. **266-269**, 520 (1999).

31. R. Nicholson and J. Walls, *FIM studies of the lattice damage in tungsten following low-energy helium ion bombardment*, J. Nucl. Mater. **76-77**, 251 (1978).

32. F. Maury, M. Biget, P. Vajda, A. Lucasson, and P. Lucasson, *Frenkel pair creation and stage I recovery in W crystals irradiated near threshold*, Radiat. Eff. Defect S. **38**, 53 (1978).

33. J. F. Ziegler, SRIM software package, available online http://www.srim.org .

34. K. Christmann, *Interaction of hydrogen with solid surfaces*, Surf. Sci. Rep. **9**, 1 (1988).

35. P. W. Tamm and L. D. Schmidt, *Interaction of H_2 with (100)W. I. Binding States*, J. Chem. Phys. **51**, 5352 (1969).

36. P. W. Tamm and L. D. Schmidt, *Binding States of Hydrogen on Tungsten*, J. Chem. Phys. **54**, 4775 (1971).

37. H. Eleveld and A. van Veen, *Deuterium interaction with impurities in tungsten studied with TDS*, J. Nucl. Mater. **191-194**, 433 (1992).

38. A. Smith, R. Barker, and P. Estrup, *Desorption of hydrogen from tungsten (100)*, Surf. Sci. **136**, 327 (1984).

39. H. W. Werner, *Quantitative secondary ion mass spectrometry: A review*, Surf. Interface Anal. **2**, 56 (1980).

40. C. W. Magee and R. E. Honig, *Depth profiling by SIMS - depth resolution, dynamic range and sensitivity*, Surf. Interface Anal. **4**, 35 (1982).

41. K. Wittmaack, *Towards the ultimate limits of depth resolution in sputter profiling: Beam-induced chemical changes and the importance of sample quality*, Surf. Interface Anal. **21**, 323 (1994).

42. D. E. Carlson and C. W. Magee, *A SIMS analysis of deuterium diffusion in hydrogenated amorphous silicon*, Appl. Phys. Lett. **33**, 81 (1978).

43. W. E. Kunz, *Deuterium ^3He Reaction*, Phys. Rev. **97**, 456 (1955).

44. W. Möller and F. Besenbacher, *A note on the ^3He + D nuclear-reaction cross section*, Nucl. Instr. Meth. **168**, 111 (1980).

45. J. L. Yarnell, R. H. Lovberg, and W. R. Stratton, *Angular Distribution of the Reaction $He^3(d,p)He^4$ between 240 keV and 3.56 MeV*, Phys. Rev. **90**, 292 (1953).

46. T. W. Bonner, J. P. Conner, and A. B. Lillie, *Cross Section and Angular Distribution of the $He^3(d,p)He^4$ Nuclear Reaction*, Phys. Rev. **88**, 473 (1952).

47. K. Albe, K. Nordlund, and R. S. Averback, *Modeling the metal-semiconductor interaction: Analytical bond-order potential for platinum-carbon*, Phys. Rev. B **65**, 195124 (2002).

48. N. Juslin, P. Erhart, P. Träskelin, J. Nord, K. O. E. Henriksson, K. Nordlund, E. Salonen, and K. Albe, *Analytical interatomic potential for modeling nonequilibrium processes in the W–C–H system*, J. Appl. Phys. **98**, 123520 (2005).

49. P. Hohenberg and W. Kohn, *Inhomogeneous Electron Gas*, Phys. Rev. **136**, B864 (1964).

50. W. Kohn and L. J. Sham, *Self-Consistent Equations Including Exchange and Correlation Effects*, Phys. Rev. **140**, A1133 (1965).

51. G. Mills, H. Jonsson, and G. K. Schenter, *Reversible work transition state theory: application to dissociative adsorption of hydrogen*, Surf. Sci. **324**, 305 (1994).

52. H. Jonsson, G. Mills, and K. W. Jacobsen, in *Classical and Quantum Dynamics in Condensed Phase Simulations*, edited by B. J. Berne, G. Ciccotti, and C. F. Coker (World Scientific, AD-DRESS, 1998).

53. H. Eyring, *The Activated Complex in Chemical Reactions*, J. Chem. Phys. **3**, 107 (1935).

54. H. Eyring, *The Theory of Absolute Reaction Rates*, T. Faraday Soc. **34**, 41 (1938).

55. E. Wigner, *Über das Überschreiten von Potentialschwellen bei chemischen Reaktionen*, Z. Phys. Chem. **B 19**, 203 (1932).

56. E. Wigner, *The Transition State Method*, T. Faraday Soc. **34**, 29 (1938).

57. N. Sandberg, B. Magyari-Köpe, and T. R. Mattsson, *Self-Diffusion Rates in Al from Combined First-Principles and Model-Potential Calculations*, Phys. Rev. Lett. **89**, 065901 (2002).

58. M. Mantina, Y. Wang, R. Arroyave, L. Q. Chen, Z. K. Liu, and C. Wolverton, *First-Principles Calculation of Self-Diffusion Coefficients*, Phys. Rev. Lett. **100**, 215901 (2008).

59. P. G. Sundell and G. Wahnström, *Self-trapping and diffusion of hydrogen in Nb and Ta from first principles*, Phys. Rev. B **70**, 224301 (2004).

60. D. E. Jiang and E. A. Carter, *Diffusion of interstitial hydrogen into and through bcc Fe from first principles*, Phys. Rev. B **70**, 064102 (2004).

61. G. Henkelman, A. Arnaldsson, and H. Jónsson, *Theoretical calculations of CH_4 and H_2 associative desorption from Ni(111): Could subsurface hydrogen play an important role?*, J. Chem. Phys. **124**, 044706 (2006).

62. G. H. Vineyard, *Frequency factors and isotope effects in solid state rate processes*, J. Phys. Chem. Solids **3**, 121 (1957).

63. C. Wert and C. Zener, *Interstitial Atomic Diffusion Coefficients*, Phys. Rev. **76**, 1169 (1949).

64. C. Wert, *Diffusion Coefficient of C in α-Iron*, Phys. Rev. **79**, 601 (1950).

65. C. Zener, in *Imperfections in Nearly Perfect Crystals*, edited by W. Shockley, J. H. Hollomon, R. Maurer, and F. Seitz (Wiley and Sons, New York, 1952).

66. J. Philibert, *Atom movements: Diffusion and mass transport in solids* (Les Éditions de Physique, France, 1991).

67. A. Einstein, *Über die von der molekularkinetischen Theorie der Wärme geforderte Bewegung von in ruhenden Flüssigkeiten suspendierten Teilchen*, Ann. Phys.-Berlin **17**, 549 (1905).

68. G. E. Moore and F. C. Unterwald, *Thermal Dissociation of Hydrogen*, J. Chem. Phys. **40**, 2639 (1964).

69. L. N. Ryabchikov, Ukr. Fiz. Zh. **9**, 293 (1964).

70. R. Frauenfelder, *Solution and Diffusion of Hydrogen in Tungsten*, J. Vac. Sci. Technol. **6**, 388 (1969).

71. A. P. Zakharov, V. M. Sharapov, and E. I. Evko, *Hydrogen permeability of mono- and poly-crystals of molybdenum and tungsten*, Fiz. Khim. Mekh. Mater. **9**, 29 (1973).

72. C. García-Rosales, P. Franzen, H. Plank, J. Roth, and E. Gauthier, *Re-emission and thermal des-orption of deuterium from plasma sprayed tungsten coatings for application in ASDEX-upgrade*, J. Nucl. Mater. **233-237**, 803 (1996).

73. P. Franzen, C. Garcia-Rosales, H. Plank, and V. K. Alimov, *Hydrogen trapping in and release from tungsten: Modeling and comparison with graphite with regard to its use as fusion reactor material*, J. Nucl. Mater. **241-243**, 1082 (1997).

74. G. Benamati, E. Serra, and C. H. Wu, *Hydrogen and deuterium transport and inventory param-eters through W and W-alloys for fusion reactor applications*, J. Nucl. Mater. **283-287**, 1033 (2000).

75. E. Serra, G. Benamati, and O. V. Ogorodnikova, *Hydrogen isotopes transport parameters in fusion reactor materials*, J. Nucl. Mater. **255**, 105 (1998).

76. R. A. Causey and T. J. Venhaus, *The use of tungsten in fusion reactors: a review of the hydrogen retention and migration properties*, Phys. Scripta **T94**, 9 (2001).

77. H. Eleveld and A. van Veen, *Void growth and thermal desorption of deuterium from voids in tungsten*, J. Nucl. Mater. **212-215**, 1421 (1994).

78. K. B. Blodgett and I. Langmuir, *Accommodation Coefficient of Hydrogen; A Sensitive Detector of Surface Films*, Phys. Rev. **40**, 78 (1932).

79. P. W. Tamm and L. D. Schmidt, *Interaction of H_2 with (100)W. II. Condensation*, J. Chem. Phys. **52**, 1150 (1970).

80. P. W. Tamm and L. D. Schmidt, *Condensation of Hydrogen on Tungsten*, J. Chem. Phys. **55**, 4253 (1971).

81. T. E. Felter, R. A. Barker, and P. J. Estrup, *Phase Transition on Mo(100) and W(100) Surfaces*, Phys. Rev. Lett. **38**, 1138 (1977).

82. M. K. Debe and D. A. King, *Space-Group Determination of the Low-Temperature $W\{001\}(\sqrt{2} \times \sqrt{2})R45°$*, Phys. Rev. Lett. **39**, 708 (1977).

83. D. A. King and G. Thomas, *Displacive surface phases formed by hydrogen chemisorption on $W\{001\}$*, Surf. Sci. **92**, 201 (1980).

84. R. DiFoggio and R. Gomer, *Tunneling of Hydrogen in Surface Diffusion on the Tungsten (110) Plane*, Phys. Rev. Lett. **44**, 1258 (1980).

85. J. W. Chung, S. C. Ying, and P. J. Estrup, *Reconstruction of the W(110) surface induced by hydrogen adsorption*, Phys. Rev. Lett. **56**, 749 (1986).

86. M. S. Altman, P. J. Estrup, and I. K. Robinson, *Multilayer reconstruction of the W(001) surface*, Phys. Rev. B **38**, 5211 (1988).

87. N. A. W. Holzwarth, J. A. Chervenak, C. J. Kimmer, Y. Zeng, W. Xu, and J. Adams, *Multilayer-relaxation geometry and electronic structure of a W(111) surface*, Phys. Rev. B **48**, 12136 (1993).

88. K. A. Muttalib and J. Sethna, *Coverage dependence and isotope effect in quantum surface diffusion*, Phys. Rev. B **32**, 3462 (1985).

89. K. O. E. Henriksson, K. Vörtler, S. Dreissigacker, K. Nordlund, and J. Keinonen, *Sticking of atomic hydrogen on the tungsten (001) surface*, Surf. Sci. **600**, 3167 (2006).

90. H. F. Busnengo and A. E. Martínez, *H_2 Chemisorption on W(100) and W(110) Surfaces*, J. Phys. Chem. C **112**, 5579 (2008).

91. X. Zhou and J. L. Erskine, *Surface core-level shifts at vicinal tungsten surfaces*, Phys. Rev. B **79**, 155422 (2009).

92. L. Cai, M. S. Altman, E. Granato, T. Ala-Nissilä, S. C. Ying, and X. Xiao, *Surface Diffusion Anomaly near a Substrate Phase Transition: H on $W(100)$*, Phys. Rev. Lett. **88**, 226105 (2002).

93. V. K. Alimov and J. Roth, *Hydrogen isotope retention in plasma-facing materials: review of recent experimental results*, Phys. Scripta **T128**, 6 (2007).

94. M. Mayer, E. Gauthier, K. Sugiyama, and U. von Toussaint, *Quantitative depth profiling of deuterium up to very large depths*, Nucl. Instr. Meth. Phys. Res. B **267**, 506 (2009).

95. A. A. Pisarev, A. V. Varava, and S. K. Zhdanov, *Ion implantation of deuterium in tungsten*, J. Nucl. Mater. **220-222**, 926 (1995).

96. R. A. Anderl, R. J. Pawelko, and S. T. Schuetz, *Deuterium retention in W, W1%La, C-coated W and W_2C*, J. Nucl. Mater. **290-293**, 38 (2001).

97. O. V. Ogorodnikova, J. Roth, and M. Mayer, *Deuterium retention in tungsten in dependence of the surface conditions*, J. Nucl. Mater. **313-316**, 469 (2003).

98. J. P. Sharpe, R. D. Kolasinski, M. Shimada, P. Calderonia, and R. A. Causey, *Retention behavior in tungsten and molybdenum exposed to high fluences of deuterium ions in TPE*, J. Nucl. Mater. **390-391**, 709 (2009).

99. F. C. Tompkins, *Chemisorption of gases on metals* (Academic Press, London, 1978).

100. P. M. Derlet, D. Nguyen-Manh, and S. L. Dudarev, *Multiscale modeling of crowdion and vacancy defects in body-centered-cubic transition metals*, Phys. Rev. B **76**, 054107 (2007).

101. S. Nagata, K. Takahiro, S. Horiike, and S. Yamaguchi, *Retention and release of deuterium implanted in Mo and W*, J. Nucl. Mater. **266-269**, 1151 (1999).

102. C.-C. Fu, J. D. Torre, F. Willaime, J.-L. Bocquet, and A. Barbu, *Multiscale modelling of defect kinetics in irradiated iron*, Nat. Mater. **4**, 68 (2005).

103. K. Heinola and T. Ahlgren, (2010), *To be published.*

104. D. Nguyen-Manh, A. P. Horsfield, and S. L. Dudarev, *Self-interstitial atom defects in bcc transition metals: Group-specific trends*, Phys. Rev. B **73**, 020101 (2006).

105. R. M. Scanlan, D. L. Styris, and D. N. Seidman, *An in situ field ion microscope study of irradiated tungsten I. Experimental results*, Phil. Mag. **23**, 1439 (1971).

106. R. M. Scanlan, D. L. Styris, and D. N. Seidman, *An in situ field ion microscope study of irradiated tungsten II. Analysis and interpretation*, Phil. Mag. **23**, 1459 (1971).

107. S. Okuda and H. Mizubayashi, *Free migration of interstitials in tungsten*, Phys. Rev. Lett. **34**, 815 (1975).

108. D. N. Seidman, K. L. Wilson, and C. H. Nielsen, *Comment on "Free migration of interstitials in tungsten"*, Phys. Rev. Lett. **35**, 1041 (1975).

109. F. Dausinger and H. Schultz, *Long-Range Migration of Self-Interstitial Atoms in Tungsten*, Phys. Rev. Lett. **35**, 1773 (1975).

110. J. R. Townsend, M. Schildcrout, and C. Reft, *Mechanical studies of irradiation-induced defects in Cu and W*, Phys. Rev. B **14**, 500 (1976).

111. K. L. Wilson, M. I. Baskes, and D. N. Seidman, *An in-situ field-ion microscope study of the recovery behavior of ion-irradiated tungsten and tungsten alloys*, Acta Metall. **28**, 89 (1980).

112. H. Tanimoto, H. Mizubayashi, H. Nishimura, and S. Okuda, *A study of self-interstitial atom in W by means of low-temperature irradiations*, Journal de Physique IV **6**, 285 (1996).

113. T. Ahlgren, K. Heinola, and K. Vörtler, (2010), *To be published.*

114. J. R. Fransens, M. S. A. E. Keriem, and F. Pleiter, *Hydrogen-vacancy interaction in tungsten*, J. Phys.: Condens. Matter **3**, 9871 (1991).